

Published in final edited form as:

Nature. 2019 July 01; 571(7766): 580–583. doi:10.1038/s41586-019-1391-0.

Conformation space of a heterodimeric ABC exporter under turnover conditions

Susanne Hofmann^{#1}, Dovile Janulienė^{#2}, Ahmad R. Mehdipour^{#3}, Christoph Thomas¹, Erich Stefan¹, Stefan Brüchert¹, Benedikt T. Kuhn¹, Eric R. Geertsma¹, Gerhard Hummer^{3,4}, Robert Tampé^{1,*}, Arne Moeller^{2,*}

¹Institute of Biochemistry, Biocenter, Goethe University Frankfurt, Max-von-Laue-Str. 9, 60438 Frankfurt/M., Germany

²Department of Structural Biology, Max-Planck-Institute of Biophysics, Max-von-Laue-Str. 3, 60438 Frankfurt/M., Germany

³Department of Theoretical Biophysics, Max-Planck-Institute of Biophysics, Max-von-Laue-Str. 3, 60438 Frankfurt/M., Germany

⁴Institute of Biophysics, Goethe University Frankfurt, Max-von-Laue-Str. 1, 60438 Frankfurt/M., Germany

These authors contributed equally to this work.

Abstract

Cryo-electron microscopy (cryo-EM) has the capacity to capture molecular machines in action^{1–3}. ATP-binding cassette (ABC) exporters are highly dynamic membrane proteins that extrude a wide range of substances from the cytosol^{4–6} and thereby contribute to essential cellular processes, adaptive immunity, and multidrug resistance^{7,8}. Despite their vital importance, the coupling of nucleotide binding, hydrolysis, and release to the conformational dynamics remains poorly resolved, especially for heterodimeric/asymmetric ABC exporters that abound in humans.

Users may view, print, copy, and download text and data-mine the content in such documents, for the purposes of academic research, subject always to the full Conditions of use:http://www.nature.com/authors/editorial_policies/license.html#terms

*Correspondence and requests for materials should be addressed to R.T. tampe@em.uni-frankfurt.de and A.M. arne.moeller@biophys.mpg.de.

Data availability. All nine three-dimensional cryo-EM density maps of the heterodimeric/asymmetric ABC transporter TmrAB in nanodiscs have been deposited in the Electron Microscopy Data Bank under accession numbers EMD-4773-81 (see ED Table 1). Atomic coordinates for the atomic models have been deposited in the Protein Data Bank under accession numbers 6RAF, 6RAG, 6RAH, 6RAI, 6RAJ, 6RAK, 6RAL, 6RAM, 6RAN. All other data are available from the corresponding authors upon reasonable request.

Author contributions. S.H. prepared all TmrAB samples and performed nucleotide occlusion, ATP hydrolysis, and transport experiments. S.H. and D.J. performed the negative-stain EM analyses. D.J. and A.M. carried out all cryo-EM imaging and single-particle analyses. A.R.M. and G.H. performed and analyzed the MD simulations. A.R.M. and C.T. built the structural models. B.T.K. and E.G. generated and selected nanobodies, and performed their characterization together with S.B., E.S. and S.H.. S.H. and S.B. generated, purified and characterized all mutants. S.H., D.J., A.R.M., G.H., R.T. and A.M. interpreted the data and wrote the manuscript with contributions from all authors. R.T. and A.M. conceived the study, designed the research, and planned the experiments. R.T. initiated, planned, and coordinated the project.

Author information. Reprints and permissions information is available at www.nature.com/reprints.

The authors declare that no competing interests exist.

Readers are welcome to comment on the online version of the paper.

Publisher's note: Springer Nature remains neutral with regard to jurisdictional claims in published maps and institutional affiliations.

Here, we present eight high-resolution cryo-EM structures that delineate the full functional cycle of an asymmetric ABC exporter in lipid environment. Cryo-EM analysis under active turnover conditions reveals distinct inward-facing (IF) conformations, one of them with bound peptide substrate, and previously undescribed asymmetric post-hydrolysis states with dimerized nucleotide-binding domains (NBDs) and a closed extracellular gate. Capturing an outward-facing (OF) open conformation requires a slow-down in ATP hydrolysis, indicating the transient nature of this state vulnerable to substrate re-entry. ATP-bound pre-hydrolysis and vanadate-trapped states are conformationally equivalent and both comprise co-existing OF conformations with open and closed extracellular gates. In contrast, the post-hydrolysis states from the turnover experiment exhibit asymmetric ADP/ATP occlusion after phosphate release from the canonical site and display a progressive separation of the nucleotide-binding domains and unlocking of the intracellular gate. Our findings reveal that phosphate release, not ATP hydrolysis, triggers the return of the exporter to the IF conformation. By mapping the conformational landscape during active turnover, aided by mutational and chemical modulation of kinetic rates to trap the key intermediates, we resolved fundamental and so-far hidden steps of the substrate translocation cycle of asymmetric ABC transporters.

ABC transporters constitute a ubiquitous superfamily of membrane proteins that shuttle a multitude of chemically diverse substrates across cell membranes⁴⁻⁶. In humans, ABC transporters typically act as promiscuous exporters, responsible for many physiological processes, multidrug resistance, and severe diseases, such as cystic fibrosis, hypercholesterolemia, lipid trafficking disorders, and immunodeficiency⁹. In all ABC transporters, two highly conserved NBDs mechanochemically couple ATP binding and hydrolysis to two transmembrane domains (TMDs) that provide a framework for substrate uptake and release on opposite sides of the membrane⁴⁻⁶. Substrate transport necessitates major conformational changes between IF and OF^{open} states. Presently available high-resolution data are dominated by snapshots of different homodimeric ABC exporters in a single nucleotide-free IF state, which cannot reveal the highly dynamic nature of individual ABC exporters. Moreover, structural information is especially limited for heterodimeric/asymmetric systems with a canonical (catalytically active) and non-canonical (inactive) ATP-binding site, which are typically found in higher eukaryotes. Major open questions concern the ATP-bound and hydrolysis transition states as well as the mechanochemical events that trigger the large-scale conformational changes during the translocation cycle.

We used cryo-EM to delineate the conformational space of a heterodimeric ABC exporter under turnover conditions (Fig. 1 and Supplementary Video 1 and 2). We examined *Thermus thermophilus* multidrug resistance proteins A and B (TmrAB) as a model system of human transporter associated with antigen processing (TAP1/2). TmrAB exhibits a broad substrate spectrum and can restore antigen presentation in human TAP-deficient cells¹⁰⁻¹². For the turnover experiment (designated TmrAB_{turnover}), TmrAB was reconstituted in lipid nanodiscs (Extended Data Fig. 1) and incubated with Mg-ATP and a fluorescent peptide (RRY(C^{Fluorescein})KSTEL, C4F) as substrate. To break the pseudo-twofold symmetry of TmrAB, we selected a high-affinity conformationally non-selective nanobody, which forms a stable complex with the NBD of TmrB without affecting the transport rates (Fig. 1 and Extended Data Fig. 2).

Cryo-EM analysis of TmrAB_{turnover} revealed a set of two distinct IF conformations (IF^{wide} and IF^{narrow}; Fig. 1a) as well as two asymmetric conformations with dimerized NBDs and a tightly sealed extracellular gate (UR^{asym} and UR^{asym*}; Fig. 1d). Both IF conformations contain two nucleotides, but free ATP/ADP exchange prevents a clear assignment. In IF^{wide}, the intracellular gate widened by 4.4 Å compared to IF^{narrow}, and the intracellular cavity increased from 4,650 to 5,900 Å³, largely because transmembrane helix six (TM6) moved (Fig. 2a-c; Supplementary Video 2). The NBDs retain their center distance despite a small sliding motion. Molecular dynamics (MD) simulations indicate a dynamic equilibrium between IF^{narrow} and IF^{wide}, showing two full transitions from IF^{wide} to IF^{narrow} and transient excursions from IF^{narrow} towards IF^{wide} (Extended Data Fig. 7d).

Intriguingly, a weak additional density close to residues M139^{TmrB} and W297^{TmrB} in IF^{wide} indicates the presence of substrate. No such density was found in IF^{narrow}, where, due to the inward movement of TM6, the smaller volume of the cavity prevents binding of bulky substrates. A prominent extra density was present at the same position in IF^{wide} from an experiment in the absence of ATP and with ten-fold higher C4F concentration (TmrAB_{C4F}) compared to TmrAB_{turnover} (Fig. 2c,d). The higher substrate concentration increased the population ratio IF^{wide}:IF^{narrow} from 1:1 to 4:1 (Extended Data Fig. 3b), indicating that peptide binding stabilizes the IF^{wide} conformation. The extra density in the central cavity is framed by the tightly sealed extracellular gate and flanked by hydrophobic and basic residues (F257^{TmrA}, F261^{TmrA}, and R80^{TmrB}) (Fig. 2d). Although almost all transmembrane helices cradle the binding pocket, the bimodal TM6 appears to be the gatekeeper for substrate binding (Fig. 2a,c). We did not model the peptide into the substrate density, as it is not fully defined, perhaps reflecting peptide flexibility, partial occupancy, or multiple binding modes, consistent with the function of multidrug transporters^{13,14}. To verify that this density corresponds to C4F, we performed single-alanine substitutions of M139^{TmrB} and W297^{TmrB}, leading to a strong reduction in substrate binding (Fig. 2e). Replacement of both residues reduced the peptide affinity in binding and transport, indicating an additive effect (Fig. 2e,f). As expected, no density for C4F was present in an apo control experiment (TmrAB_{apo}) (Extended Data Fig. 3), while both IF conformations were still found. In summary, this suggests conformation-selective but not conformation-inducing substrate binding.

Substrate release requires an OF^{open} conformation. However, we were unable to resolve this state in TmrAB_{turnover}, which indicates that the OF^{open} conformation must be highly transient, possibly to prevent substrate re-entry at the extracellular gate after release¹⁵. We stabilized the OF^{open} conformation by mutating the catalytic base (E523Q^{TmrA}), thereby allowing ATP binding but reducing the rate of ATP hydrolysis (Extended Data Fig. 1c,d) and accordingly increasing the half-life of the exporter in the ATP-bound state upon addition of Mg-ATP (TmrA^{EQB}_{ATP}). Remarkably, within the same dataset, we resolved two different OF conformations, OF^{open} and OF^{occluded}, both with bound ATP (Fig. 1b and Fig. 3a). OF^{occluded} is related to the previously reported structure of homodimeric McjD in the presence of the non-hydrolysable ATP-analog AMP-PNP¹⁶ (Extended Data Fig. 7), albeit with a significantly smaller cavity for substrate binding (~3,400 Å³) that is insufficient to accommodate bulky peptides. The second conformation displays a wide opening of the TMDs into the extracellular space, resembling the reported structure for homodimeric Sav1866^{17,18}

(Fig. 1 and Extended Data Fig. 7), suggesting that binding of two ATP molecules is sufficient to drive the large-scale conformational change from IF to OF^{open}.

To explore the effect of nucleotide hydrolysis on the conformation space, we trapped TmrAB by orthovanadate (V_i), mimicking the hydrolysis transition state (TmrAB_{ATP- V_i}). As for TmrA^{EQB}_{ATP}, we observed two populations, representing the OF^{open} and OF^{occluded} conformations (Fig. 1c). In both maps, ATP was occluded at the non-canonical site, while the canonical site contained ADP-vanadate (Fig. 3a,b). The simultaneous occlusion of one ATP and one ADP in the V_i -trapped state was further demonstrated by radiotraced [α -³²P]ATP (Fig. 3c). We identified possible pathways for inorganic phosphate (P_i) release and V_i entry in MD simulations of OF^{occluded} with ADP+ P_i in the canonical site (see Methods). Two water-filled tunnels connected P_i to the bulk solvent independent of its protonation state (Fig. 3d). The pathway towards the coupling helix has been previously reported¹⁹; however, a detailed characterization of the P_i release mechanism requires further studies. Within the same dataset, the organization of the NBDs in OF^{open} and OF^{occluded} is identical, indicating that the motion of the extracellular gate is uncoupled from NBDs in the nucleotide-bound state. Furthermore, no significant differences for the individual conformers were observed between the two different TmrAB_{ATP- V_i} and TmrA^{EQB}_{ATP} datasets (Extended Data Table 2), suggesting the equivalence of the ATP-bound and vanadate-trapped states as shown for type I/II ABC importers MalFGK₂, BtuC₂D₂, and human P-gp^{20–22}.

Intriguingly, the two TmrAB_{turnover} conformations with dimerized NBDs are markedly different from all other structures. Here, the canonical site is slightly wider and contains ADP, while ATP is still bound at the non-canonical site, demonstrating an asymmetric post-hydrolysis state (Fig. 1d and Fig. 3a). In these new asymmetric unlocked-return conformations (UR^{asym} and UR^{asym*}), 1.5–3.0 Å motions of TM3 and TM4 unlocked the intracellular gate, indicating a progressive return to the IF conformation (Fig. 3e,f). To exclude that the asymmetric state can be induced through a backward reaction from an IF conformation by simultaneous binding of ATP and ADP, we performed an experiment using an equimolar ratio of ATP and ADP on the TmrA^{EQB} mutant (TmrA^{EQB}_{ATP-ADP}). The cryo-EM analysis of this sample resulted in a set of four structures: OF^{open} and OF^{occluded} with symmetrical ATP occupancy, as well as IF^{wide} and IF^{narrow} with bound ADP; however, no UR^{asym} was detected. As ATP hydrolysis at the non-canonical site is unlikely¹⁰, the observed UR^{asym} conformations of TmrAB_{turnover} must therefore represent post-ATP-hydrolysis states. This in turn suggests that the trigger to reset the transporter to an IF conformation is P_i release, in analogy to the ATP synthase rotation and SecA-dependent protein translocation^{23–25}. The dilation of the intracellular gate in UR^{asym} and UR^{asym*} prohibits the opening of the extracellular gate and sets the transporter on path to the IF conformations.

Our eight high-resolution structures reveal the translocation and ATP hydrolysis cycle of a heterodimeric ABC exporter in unprecedented detail (Fig. 4). In the IF state, TM6 acts as a gatekeeper controlling access to the intracellular cavity for conformation-specific substrate uptake. ATP binding to the NBDs and the resulting NBD dimerization allow the extracellular gate to open. In the resulting OF state, the transporter can transition between

OF^{open} and OF^{occluded} conformations until the release of P_i from the canonical site weakens the NBD interactions. In turn, the intracellular gate unlocks, and the transporter transitions from an OF to an IF conformation via UR^{asym}. The high abundance of the asymmetric ADP/ATP-bound UR^{asym} state under turnover conditions with excess of ATP suggests that the separation of the sandwiched NBD dimer, which requires dissociation of the ATP-bound non-canonical site, constitutes the rate-limiting step during the translocation cycle. Our cryo-EM approach under turnover conditions extends the mechanistic understanding of heterodimeric ABC export systems and may serve as a general template for the analysis of ABC transporters and other molecular machines.

Methods

No statistical methods were used to predetermine sample size. The experiments were not randomized. The investigators were not blinded to allocation during experiments and outcome assessment.

Production and purification of TmrAB

Expression and purification of TmrAB was performed as described¹⁰. TmrAB was produced in *E. coli* BL21(DE3) grown in LB high salt media at 37 °C and induced with 0.5 mM IPTG. Harvested cells, resuspended in lysis buffer (20 mM HEPES-NaOH pH 7.5, 300 mM NaCl, 50 µg/ml lysozyme, 0.2 mM PMSF), were disrupted by sonication and membranes pelleted at 100,000 x g for 45 min at 4 °C. To extract TmrAB, crude membranes were solubilized with 20 mM of β-n-dodecyl β-D-maltoside (β-DDM) in purification buffer (20 mM HEPES-NaOH pH 7.5, 300 mM NaCl, 0.2 mM PMSF). The C-terminally His₁₀-tagged TmrAB was captured using Ni-NTA agarose (Qiagen) for 60 min at 4 °C, followed by size exclusion chromatography (SEC) (TSKgel[®] G3000SW_{XL}, Tosoh Bioscience LLC) in SEC buffer (20 mM HEPES-NaOH pH 7.5, 150 mM NaCl, 1 mM β-DDM). Peak fractions were pooled for functional and structural studies.

Production and purification of MSP1D1

pMSP1D1 was a gift by Stephen Sligar (Addgene plasmid #20061). Membrane scaffold protein MSP1D1 was expressed and purified as described²⁶. In brief, MSP1D1 was expressed in *E. coli* BL21(DE3) grown in LB media supplemented with 0.5% glucose at 37 °C. At an OD₆₀₀ of 1, expression was induced with 1 mM IPTG and cells were grown for 1 h at 37 °C. Subsequently, the temperature was lowered to 28 °C and cells were grown for additional 4 h. Cells were disrupted by sonication in lysis buffer (40 mM Tris-HCl pH 8.0, 300 mM NaCl, 1% Triton X-100). The protein was purified via its N-terminal His₇-tag.

Generation and purification of nanobodies

TmrAB-specific nanobodies were generated as described^{27,28}. In brief, one alpaca (*Vicugna pacos*) was immunized six times with 100 µg of MNG-3-solubilized TmrAB at the Nanobody Service Facility, University of Zurich. Four days after the final antigen boost, peripheral blood lymphocytes were isolated, and their RNA was purified and converted into cDNA by reverse-transcription PCR. The nanobody repertoire was cloned into phage-display vector pDX, a derivative of pMESy4²⁹. Nb9F10 was identified after two rounds

of biopanning using neutravidin-captured biotinylated TmrAB. *E. coli* TG1/pDX_Nb9F10 were cultivated in TB medium supplemented with ampicillin. Cells were grown at 37 °C until an OD₆₀₀ of 1.0 was reached. Temperature was reduced to 25 °C and overnight expression was induced by the addition of 0.5 mM IPTG. Cell pellets were resuspended in 20 mM HEPES-NaOH pH 7.5, 150 mM NaCl, and 1 mM MgCl₂, and incubated for 1 h at 4 °C in the presence of 1 mg/ml lysozyme and traces of DNase I before disruption with a Stansted Homogenizer EP (Stansted Fluid Power LTD). The lysate was cleared by centrifugation, and nanobodies were purified by Ni-NTA agarose and SEC (Superdex™ 75 10/300 GL, GE Healthcare).

Reconstitution into MSP1D1 nanodiscs

Purified TmrAB and MSP1D1 were mixed with bovine brain lipid extract (Sigma-Aldrich) solubilized in 20 mM of β -DDM at a TmrAB:MSP1D1:lipid molar ratio of 1:7.5:100 in SEC buffer without detergent. After incubation at RT for 30 min, SM-2 Bio-beads™ (Bio-Rad) were added in two consecutive incubation steps to remove the detergent (1 h, overnight). TmrAB-containing nanodiscs were separated from empty discs by SEC (Superdex™ 200 Increase 3.2/300, GE Healthcare) in SEC buffer without detergent and concentrated to 5 mg/ml at 1,500 x g using Amicon® Ultra-0.5 ml centrifugal filters with a 50 kDa cut-off (Millipore). For EM, a 1.25-fold molar excess of Nb9F10 was added and incubated for 15 min on ice. TmrAB-Nb-complexes were separated from unbound Nb by SEC (KW404-4F, Shodex) in SEC buffer without detergent.

ATPase assay

TmrAB (0.2 μ M) in 1 mM of β -DDM or reconstituted into nanodiscs was incubated with 3 mM MgCl₂ and 1 mM ATP (supplemented with tracer amounts of [γ -³²P]ATP) in SEC buffer with and without detergent, respectively. Release of inorganic phosphate was monitored over a time course of 20 min at 68 °C. Reaction mixtures were analyzed by thin layer chromatography on polyethyleneimine cellulose. Data were presented as mean \pm SD ($n=3$).

Nucleotide occlusion

Bound nucleotides were identified by trapping experiments as described¹⁰. In brief, TmrAB (5 μ M) was incubated with 3 mM MgCl₂, 1 mM ATP (supplemented with tracer amounts of [α -³²P]ATP), and 5 mM orthovanadate for 3.5 min at 68 °C. Subsequently, 2 mM ATP were added and incubated for 2 min at RT. Unbound nucleotides were removed by rapid gel filtration (Micro Bio-Spin® 30, Bio-Rad). The identity of bound nucleotides was analyzed by thin layer chromatography on polyethyleneimine cellulose. Data were presented as mean \pm SD ($n=3$).

Substrate binding

Binding of fluorescent substrate was analyzed by fluorescence polarization as described¹². In a total volume of 20 μ l, TmrAB (2 μ M) was added to 50 nM of RRY(C^{Fluorescein})KSTEL (C4F) in SEC buffer. After 15 min incubation at 4 °C, fluorescence polarization was

measured using a microplate reader (CLARIOstar[®], BMG LABTECH) at $\lambda_{\text{ex/em}}=485/520$ nm. Data were presented as mean \pm SD ($n=3$).

Reconstitution and substrate transport

For substrate translocation studies, TmrAB was reconstituted into liposomes composed of *E. coli* polar lipids/DOPC in a 7:3 ratio (w/w), similar to the previously described protocol¹². In brief, SEC-purified, detergent-solubilized TmrAB was added to Triton X-100-destabilized liposomes in a 1:50 (w/w) ratio and incubated for 30 min at 4 °C. For detergent removal, SM-2 Bio beads (Bio-Rad) were added in four consecutive steps. Proteoliposomes were harvested by ultracentrifugation for 30 min at 270,000 x g and resuspended in transport buffer (20 mM HEPES-NaOH pH 7.5, 150 mM NaCl, 5% glycerol) to a final lipid concentration of 5 mg/ml. To analyze ATP-dependent transport, TmrAB-containing proteoliposomes were incubated with 0-30 μ M C4F peptide, 1 mM ATP, and 3 mM MgCl₂ for 6 min at 68 °C in transport buffer. Transport was stopped by the addition of four volumes of ice-cold stop buffer (1x PBS pH 7.5, 10 mM EDTA) and transferred onto 96-well MultiScreen[®] microfilter plates (0.65 μ m diameter, Millipore) pre-treated with 0.3% (w/v) polyethyleneimine. To remove excess of fluorescent substrate, proteoliposomes were washed twice with 250 μ l of ice-cold stop buffer. To disrupt the liposomes, 250 μ l of liposome lysis buffer (1x PBS pH 7.5, 1% SDS) were added and incubated for 10 min at RT. To quantify transported substrate, samples were measured using a microplate reader (CLARIOstar[®], BMG LABTECH) at $\lambda_{\text{ex/em}}=485/520$ nm. Samples without ATP were used as negative control and subtracted as background. Data were measured in triplicates and presented as mean \pm SD. For the determination of transport kinetics, data were fitted according to the Michaelis-Menten equation.

Cryo-EM sample preparation and data acquisition

Sample quality was routinely tested by negative-stain EM, using 2% (w/v) uranyl formate solution as previously described³⁰. Negative-stain micrographs were recorded automatically, using Legikon³¹, on a Tecnai-Spirit transmission electron microscope (Thermo Fisher), operating at 120 kV and equipped with Gatan 4x4K CCD camera at a nominal magnification of 42,000, corresponding to a pixel size of 2.68 Å/pix. For cryo-EM grid preparation, 3 μ l of 0.8-1.2 mg/ml TmrAB-Nb or TmrA^{EQB}-Nb complex (with or without nucleotides and substrate) were applied onto freshly glow-discharged Quantifoil grids with gold support (R2/2 or R1.2/1.3) and plunge-frozen in liquid ethane using a Vitrobot Mark IV (Thermo Fisher) with the environmental chamber set to 100% humidity and 4°C. For the turnover experiment, TmrAB-Nb was incubated at 45 °C with 5 mM ATP, 6 mM MgCl₂ and 50 μ M C4F peptide for 1 min and immediately plunge-frozen. For the TmrA^{EQB}_{ATP} experiment, 1 mM of ATP and 3 mM MgCl₂ was used and activation at 45 °C was extended to 5 min. The same ATP concentration and incubation time was used in the TmrAB_{ATP-V_i} experiment with addition of orthovanadate (1 mM). TmrA^{EQB}_{ATP-ADP} experiment was carried out in an identical manner with addition of 1 mM ATP and 1 mM ADP. For the TmrA^{EQB}_{C4F} dataset, TmrA^{EQB} was incubated with 500 μ M of C4F peptide for 5 min at 20 °C before plunge freezing, while the apo control was obtained by freezing TmrA^{EQB} without any additives. Micrographs (Extended Data Fig. 4) were recorded automatically with EPU, using a Titan Krios microscope (Thermo Fisher), operated at 300 kV, and equipped with a

BioQuantum energy filter and a K2 camera (Gatan), at a nominal magnification of 130,000, corresponding to a pixel size of 1.077 Å. Dose-fractionated movies were acquired at an electron flux of 9-9.5 e⁻/pixel/s over 8 s with 0.2 s exposures per frame (40 frames in total), corresponding to a total electron dose of ~62 e⁻/Å². Images were recorded in the defocus range from -0.8 to -2.8 μm. Data collection quality was monitored through Warp³².

Cryo-EM image processing

Frame-based motion correction was performed using the RELION-3³³ implementation of MotionCor2³⁴ with a dose filter of 1.5 or 1.6 e⁻/Å²/frame. The contrast transfer function (CTF) was estimated from non-dose weighted images, using Gctf³⁵ within RELION-3. Small subsets of images were initially pre-processed in either cisTEM³³ or Warp³², following data collection, and obtained particles were subjected to a likelihood based 2D classification to generate templates for automated particle selection in RELION-3. Picked particles were extracted at a box size of 64 pixels with 4.308 Å/pixel and directly subjected to a single round of multi-model 3D classification to eliminate bad picks. The cryo-EM map of TmrAB in IF conformation (EMDB 6085) was used as a starting reference¹¹. Selected maps at 8.6 Å resolution (Nyquist for the binned data) readily revealed multiple conformations (Extended Data Fig. 5, processing workflow). The selected particles from each conformation were re-centered, re-extracted at full pixel size, and subjected to another round of 3D-classification to further clean the stacks. Each conformation was then refined individually. Particles were polished and ctf refined as implemented in RELION-3. To further sort out conformational variability, refined particles were subjected to the next round of 3D classification with no alignment or using local searches. The resulting best classes were then refined and post-processed in RELION-3. In cases, where flexibility was observed, CryoSPARC³⁶ non-uniform refinement provided better resolved final maps. All FSC curves were generated in RELION-3, using unfiltered half maps either from RELION-3 or from CryoSPARC. Local resolution estimation was performed in CryoSPARC for all maps. The quality of all maps is demonstrated in Extended Data Fig. 6. No symmetry was applied at any step of processing. An exemplary processing workflow is provided in Extended Data Fig. 5 and dataset statistics in Extended Data Table 1.

Model building

To build the structural models, we used three initial models: (i) the equilibrated X-ray structure of TmrAB (PDB ID: 5MKK)¹² was used for the fitting of the IF maps. (ii) An OF^{occluded} model obtained by targeted MD to the McjD-like conformation¹⁶ (see below). This model was used for the fitting of the OF^{occluded} maps. (iii) An OF^{open} model obtained by targeted MD to the Sav1866-like conformation¹⁸ (see below). This model was used for the fitting of the OF^{open} maps. Pairwise sequence alignments of TmrAB with the target models in the respective transporter state (OF^{occluded}: McjD with PDB ID: 4PL0; OF^{open}: Sav1866 with PDB ID: 2ONJ) were generated using CLUSTALW³⁷ and applied together with the target structures to build 100 candidate models of TmrAB using Modeller 9v14³⁸. The sequence similarity between Sav1866 and TmrA and TmrB is 55% and 49%, respectively, and between McjD and TmrA and TmrB it is 37% and 40%, respectively. Extended Data Figure 7 illustrates the structural similarities of TmrAB in different states to other ABC transporters, including the homology model targets. The OF^{occluded} and OF^{open}

models with the respectively highest MODELLER score and best PROCHECK profile were then equilibrated in a membrane and used as target structures for targeted MD simulations using NAMD v2.9³⁹. Starting from the IF structure of TmrAB, a bias potential with a force constant of 500 kcal mol⁻¹ Å⁻² acting on the Ca RMSD pushed the initial structure toward the target structure. We monitored the intracellular and extracellular gate angles to ensure that the NBDs dimerize first, before the extracellular gate opens, without forming an intermediate structure open to both intracellular and extracellular side. After this 10-ns targeted MD run, two ATP nucleotides and two Mg²⁺ ions were placed in the nucleotide-binding site and the systems were equilibrated in a 10-ns run with restraints on the Ca positions to relax the lipids and water molecules around the protein. Afterwards, a 50-ns unbiased production MD run was performed for each system. The resulting structures were used as initial models for the cMDFF analysis.

Cascade MD flexible fitting (cMDFF)⁴⁰ simulations were used for the initial fit, set up with the MDFF plugin v0.4 in VMD1.9.2. The cMDFF simulations were performed in vacuum with a gscale factor of 0.3 describing the strength of the external potential derived from the EM density map. In the cMDFF simulations, the cryo-EM density maps were smoothed by applying Gaussian blurs (half-widths $\sigma = 0.5, 1, \dots, 5$ Å) to obtain a set of theoretical maps with gradually decreasing resolution. First, the models were docked rigidly into the cryo-EM density maps with Situs 2.7.2 (colores module). Afterwards, the initial docked models were fitted to the maps with $\sigma = 5$ Å. Then, the resulting adjusted models were flexibly adapted to the next higher-resolution maps in the series, ending with a fit to the unblurred cryo-EM density maps. At each step, 200 ps MDFF simulation was performed followed by 1000 steps of minimization. Restraints were used during the cMDFF simulations to enforce the original secondary structure, chirality, and isomerism. The models obtained from the cMDFF simulations were manually edited in Coot⁴¹, refined in Phenix⁴² using real-space refinement, and validated with built-in functions of Coot, with MolProbity⁴³, and PROCHECK⁴⁴. The difference density between map and model ($F_{obs} - F_{calc}$, $\Phi_{i_{obs}}$) was calculated with the real_space_diff_map tool of the Phenix software suite. The nucleotide density was extracted with the vop zone command in Chimera using a cutoff distance of 2 Å.

MD simulations

All-atom explicit solvent MD simulation was performed for the lipid-membrane embedded TmrAB structures. The TmrAB structures were embedded in a bilayer containing an equimolar mixture of POPE and POPG lipids⁴⁵, which are abundant in both, the *E. coli* expression system and the native *T. thermophilus*. The IF, OF^{occluded}, and OF^{open} systems contained 253PE/253PG, 298PE/298PG and 250PE/252PG lipids, respectively. All systems were hydrated with 150 mM NaCl electrolyte. The modified all-atom CHARMM36⁴⁶ force field was used for protein, lipids, and ions, together with TIP3P water. The MD trajectories were analyzed with Visual Molecular Dynamics (VMD). All simulations were performed using GROMACS 5.0.6⁴⁷. The starting systems were energy minimized for 5,000 steepest-descent steps, first equilibrated for 500 ps of MD in an NVT ensemble and later for 8 ns in an NPT ensemble under periodic boundary conditions. During equilibration, the restraints on the positions of non-hydrogen protein atoms of initially 4000 kJ·mol⁻¹·nm⁻² were gradually

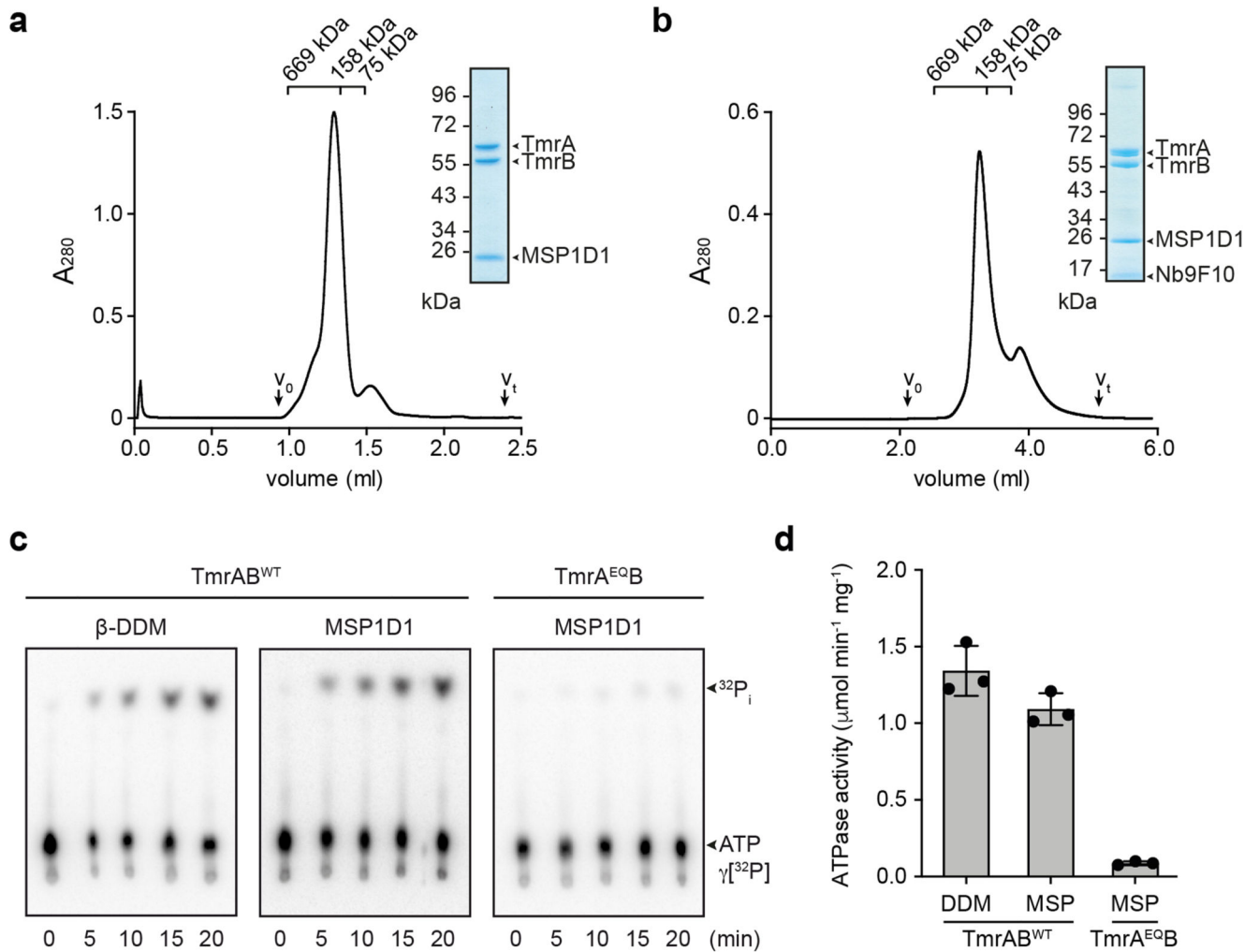
released. Particle-mesh Ewald summation with cubic interpolation and a 0.12 nm grid spacing was used to treat long-range electrostatic interactions. The time step was initially 1 fs and then increased to 2 fs. The LINCS algorithm was used to fix all bond lengths. Constant temperature was set initially with a Berendsen thermostat with a coupling constant of 1.0 ps. A semiisotropic Berendsen barostat was used to maintain a pressure of 1 bar. During the production runs, a Nosé-Hoover thermostat and a Parrinello-Rahman barostat replaced the Berendsen thermostat and barostat. Analysis was carried out on the basis of the unconstrained simulations.

IF^{wide} and IF^{narrow} from $TmrAB_{turnover}$ were each simulated at 310 K with ATP/ATP, ADP/ADP, and ADP/ATP in canonical/non-canonical sites (2x500 ns, 2x500 ns, and 2x450 ns, respectively). Hydration has been shown to affect transporter conformational equilibria^{48–50}, yet may relax only slowly on the MD time scale. However, in the IF conformations, rapid water exchange with bulk ensures ready equilibration of the cavity hydration already during the initial equilibration phase, with ~190 and ~140 water molecules in IF^{wide} and IF^{narrow} , respectively.

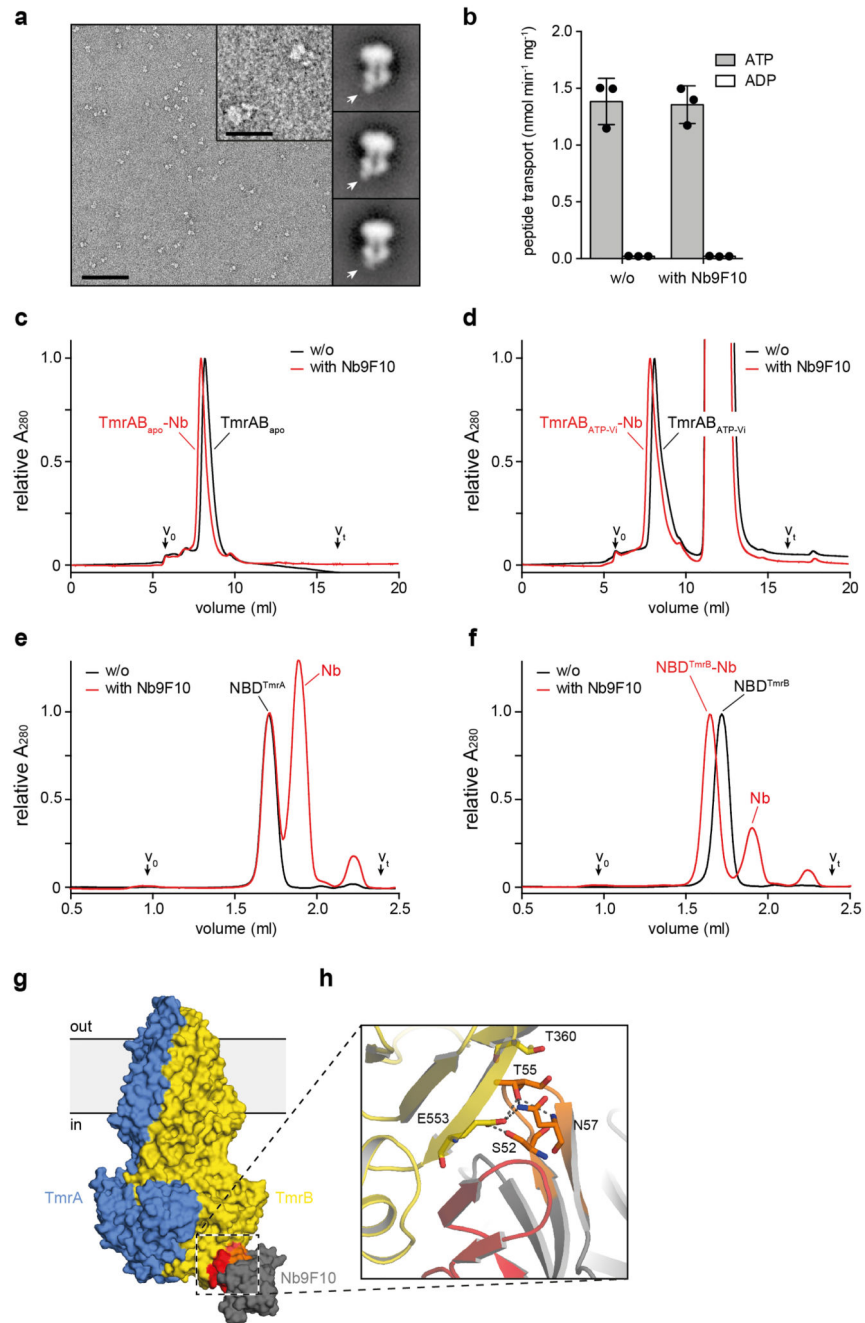
To study phosphate release by MD simulation, we replaced the vanadate molecule in the $OF^{occluded}$ structure from the $TmrAB_{ATP-V_i}$ dataset by phosphate. We identified possible phosphate release pathways by MD simulation of $OF^{occluded}$ with vanadate replaced by P_i . We performed simulations at 310 K in three different protonation states: $ADP+HPO_4^{2-}$ (610 ns), $ADP+H_2PO_4^-$ (400 ns), $ADP+H_2PO_4^- + D522^{TmrA}$ protonated (500 ns). To test for possible force-field dependencies, we also simulated the $ADP+H_2PO_4^-$ and $ADP+HPO_4^{2-}$ systems with the AMBER99-SB*-ILDN-Q force field (2x500 ns). P_i remained bound during all simulations.

The $OF^{occluded}$ and OF^{open} structures from the $TmrA^{EQB}_{ATP-ADP}$ and $TmrAB_{ATP-V_i}$ datasets were simulated at 310 K with ATP in both nucleotide sites (4x500 ns). The two UR^{asym} structures from the $TmrAB_{turnover}$ dataset were simulated with ADP/ATP in canonical/non-canonical sites, respectively (2x500 ns).

Extended Data

**Extended Data Figure 1. Reconstitution of TmrAB in lipid nanodiscs.**

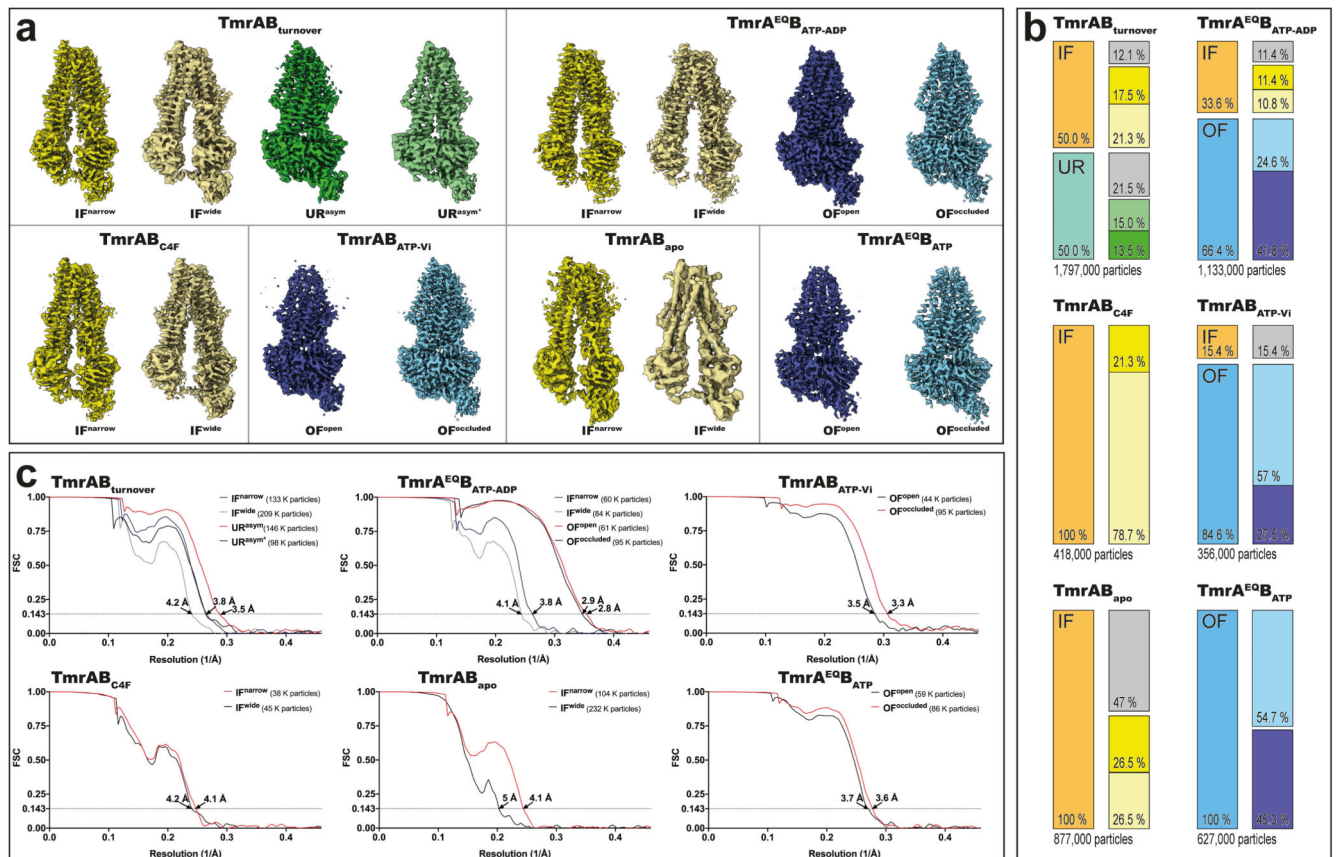
a, SEC and SDS-PAGE (Coomassie) illustrating reconstitution of TmrAB in MSP1D1 nanodiscs. Column: Superdex 200 Increase 3.2/300. **b**, Isolation of TmrAB-MSP-Nb-complex for cryo-EM. Column: Shodex KW404-4F. **c**, Time course of $[\gamma\text{-}^{32}\text{P}]\text{ATP}$ hydrolysis of detergent-solubilized and nanodisc-reconstituted TmrAB^{WT} and TmrAB^{EQB}. **d**, ATPase activity of detergent-solubilized and nanodisc-embedded TmrAB (background corrected). TmrAB^{EQB} displays a drastically decreased ATPase activity in comparison to TmrAB^{WT}. The mean \pm SD is calculated based on three different data points (time points in Figure 1c).



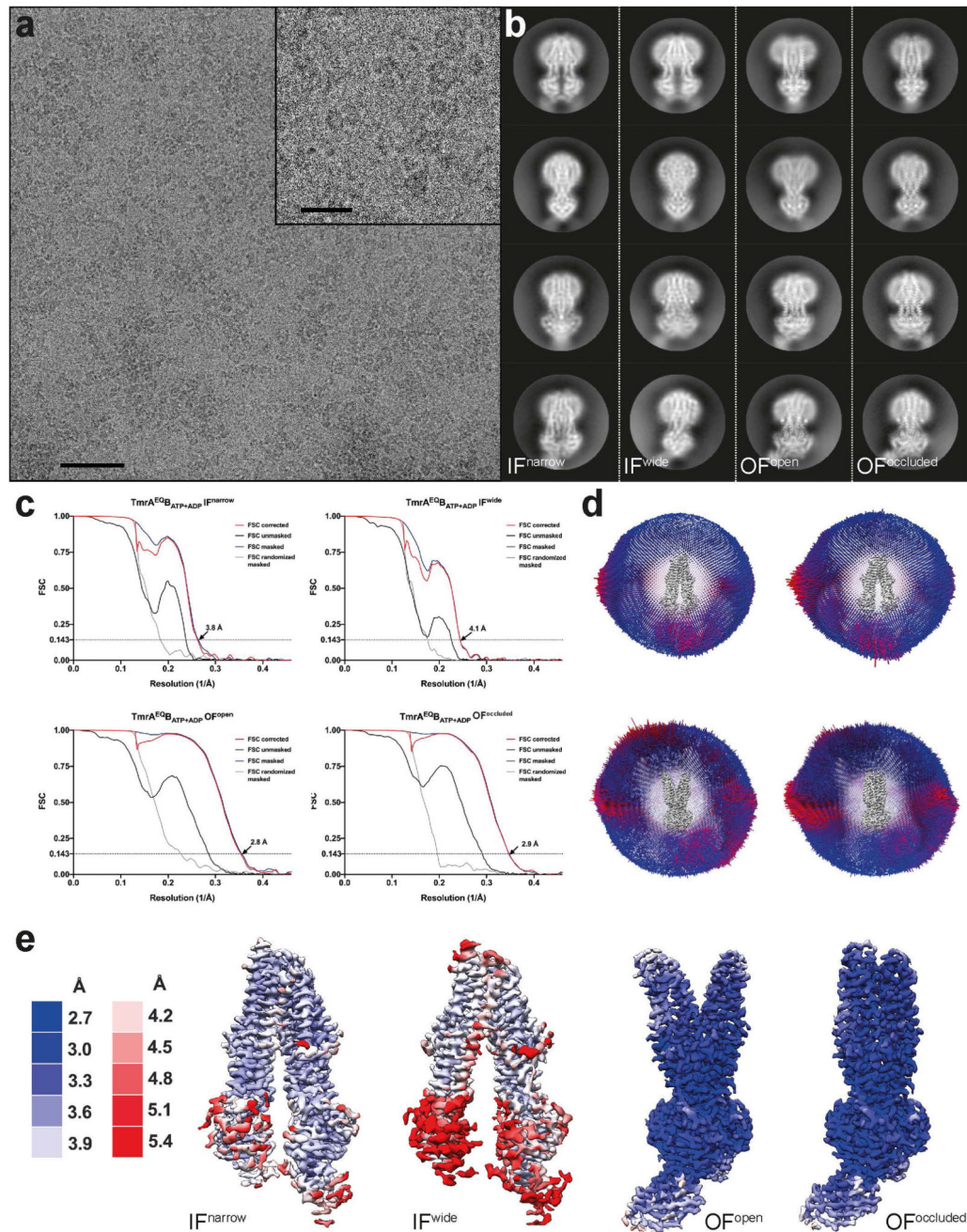
Extended Data Figure 2. TmrAB-nanobody interaction.

a, Expanded view of a representative negative-stain raw micrograph and 2D class averages of TmrAB-Nb complexes. In the 2D class averages, note the clear density for Nb9F10 bound to the intracellular side of TmrAB. The scale bar is 100 nm in the micrograph and 25 nm in the inset (magnified 4x). **b**, Peptide transport of TmrAB in proteoliposomes with and without addition of Nb9F10. Proteoliposomes were incubated with Nb9F10 (100 nM) for 15 min on ice and peptide import into proteoliposomes was subsequently followed for 8 min at 45 °C, mean \pm SD from three experiments. **c** and **d**, Nb9F10 binds the apo (**c**) and

vanadate-trapped (**d**) TmrAB. Data are normalized to apo TmrAB without Nb. Column: TSKgel G3000SW_{XL}. **e** and **f**, Nb9F10 forms a stable complex with NBD of TmrB (**f**), but not TmrA (**e**). In order to illustrate stoichiometric binding, data were normalized to the NBD^{TmrA} chromatogram without Nb. Column: Superdex 200 Increase 3.2/300. **g**, Surface representation of TmrAB and Nb9F10 colored as in Fig. 1. CDR2 and CDR3 are indicated by orange and red, respectively. **h**, Close-up view of the TmrAB-Nb9F10 interface, colored as in **g**. Polar interactions include a short β -sheet between the CDR3 loop and a β -strand of the NBD, as well as several residues of CDR2, which are shown as sticks.

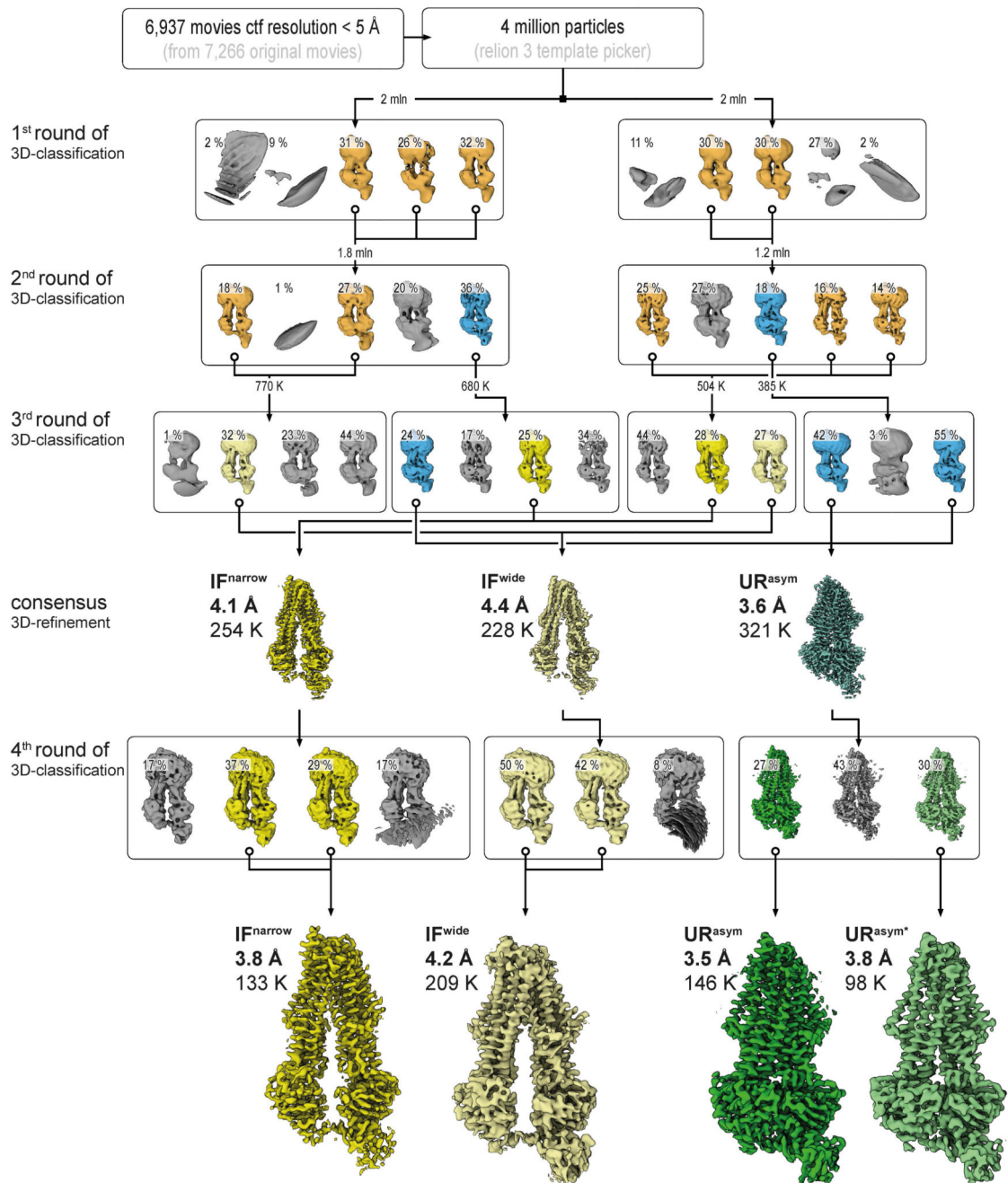


Extended Data Figure 3. Cryo-EM densities and conformational distribution from all datasets. **a**, Final maps from all datasets. In all cases, at least two conformations were observed, in accordance with the highly dynamic nature of the transporter. **b**, Particle distribution in each dataset. The first column represents the total amount of particles after two rounds of 3D classification to remove false positives. At this stage, the main OF and IF conformations were already distinguishable (IF particles, orange; OF, blue; UR, teal; also see Extended Data Fig. 5); however, no safe assignment about the sub-conformation could be made. The second column represents the distribution of each specific conformation after further sub-classification. Color code as in **a** (the two UR^{asym} conformations are colored in light and dark green, poor-quality particles in grey). **c**, FSC curves for all maps in each dataset, along with the number of particles used during the final refinement.



Extended Data Figure 4. Cryo-EM analysis of TmrA^{EQB}ATP-ADP.

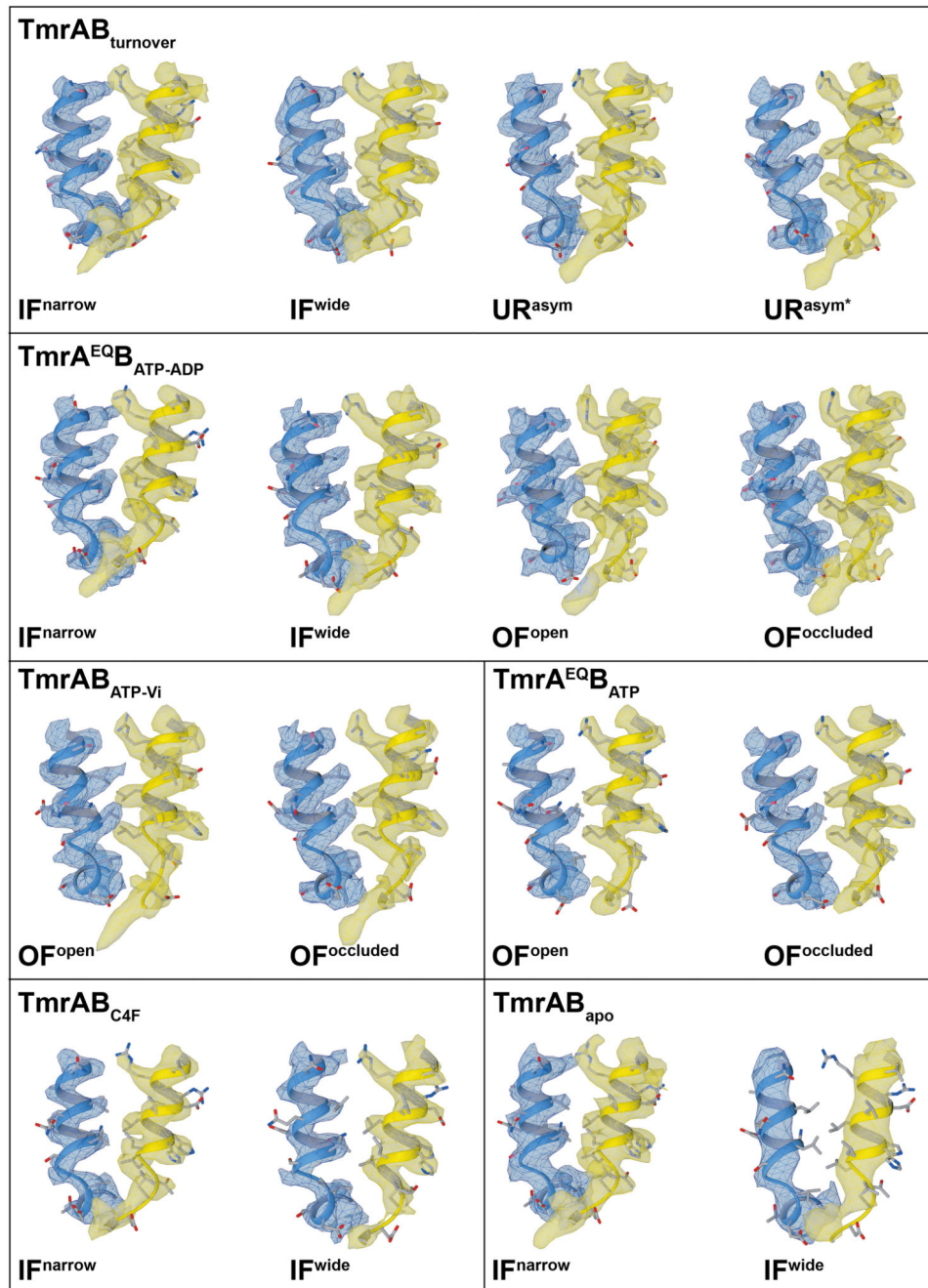
a, Typical cryo-EM micrograph. Scale bars, 50 nm in the micrograph and 20 nm in the zoom-in. **b**, Representative 2D class averages for each conformation, observed in the dataset. **c**, Fourier shell correlation (FSC) curves, generated in RELION-3, for all TmrA^{EQB}ATP-ADP maps. **d**, Angular assignment for each map. The height of individual cylinder bars is proportional to the number of particles in each view. The most frequent views are colored in red. **e**, Local resolution estimation for the four densities as estimated in CryoSPARC.



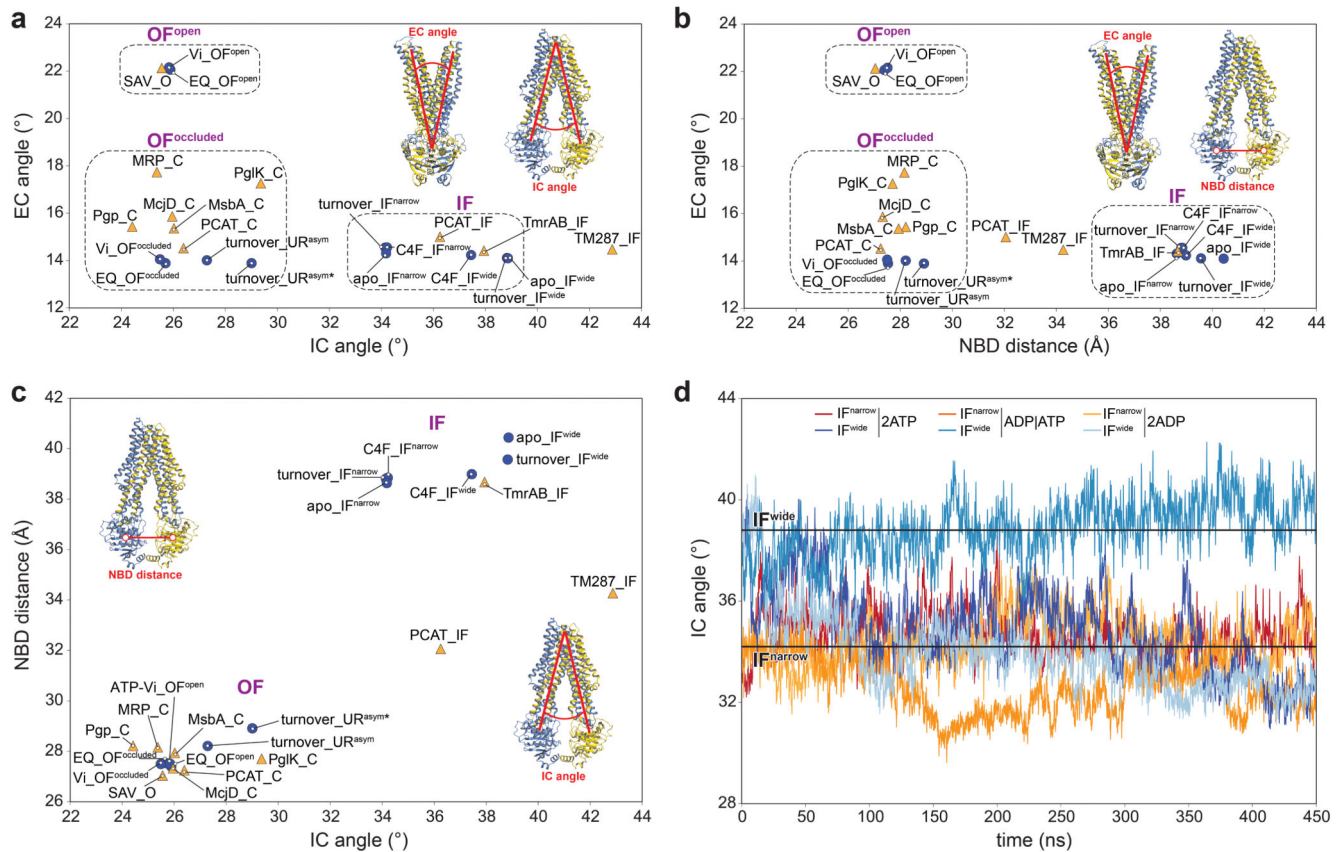
Extended Data Figure 5. Image processing workflow for TmrAB_{turnover}

From 7,266 original motion-corrected movies, 6,937 micrographs, containing signal better than 5 Å (with the majority around 3.5 Å) as estimated by Gctf³⁵, were used in processing. Four million particles were generously auto picked in RELION-3 using 2D templates, extracted at a box size of 64 pixels with 4.3 Å/pixel and directly subjected to multi-model 3D classification to eliminate false positives. To speed up the calculations and overcome large memory demands, the stack was divided into two subsets, containing two million particles each, which were processed in parallel. All maps that reached 8.6 Å resolution

(Nyquist for the binned data) were kept (orange) and the corresponding particles were re-centered, re-extracted at full pixel size and subjected to a second round of 3D classification. The selected IF (orange) and UR^{asym} (blue) particles were further subclassified. The resulting IF^{wide}, IF^{narrow}, and UR^{asym} particles were pooled and each conformation was refined separately. Particles were polished and ctf refined as implemented in RELION-3, resulting in 4.4 Å, 4.1 Å, and 3.6 Å maps, respectively. Despite the overall high-quality of the obtained densities, visual inspection still revealed significant anisotropy in the resulting volumes. We interpreted this as the result of remaining conformational variance and therefore re-classified the individual stacks to sort out conformational flexibility. To do this, the refined UR^{asym} particles were subjected to a fourth round of 3D classification with no alignment, which revealed two different UR^{asym} conformations. Both conformations were further refined using non-uniform refinement in CryoSPARC³⁶, resulting in 3.5 Å and 3.8 Å resolution maps for UR^{asym} and UR^{asym*}, respectively (shown in green). In parallel, IF particles were subjected to heterogenous refinement, followed by non-uniform refinement in CryoSPARC, which further improved the resolution to 3.8 and 4.2 Å for IF^{narrow} and IF^{wide}, respectively. Color code as in Extended Data Fig. 4. Processing workflows for all other datasets followed the same scheme with only minor modifications at the last steps of 3D classification.

**Extended Data Figure 6. Map quality.**

To demonstrate the quality of each map, a selected region, spanning residues 213-235 of TmrA and 94-106 of TmrB, was extracted from each corresponding experimental map. All maps display clear side-chain densities, except for the IF^{wide} map of the TmrAB_{apo} control, which is also the smallest dataset in size.



Extended Data Figure 7. Conformation space of type I ABC exporters.

a-c, Conformation space of the EM structures from this study and previously published ABC transporter structures is shown based on three parameters: the intracellular gate angle (IC angle), the extracellular gate angle (EC angle), and the distance between two nucleotide-binding domains (NBD distance). The EM structures, obtained in this study, are shown as blue circles, and previously published structures as orange triangles. The clustering of structures in three major conformations (IF, OF^{open}, and OF^{occluded}) is highlighted by dashed rectangles in **a** and **b**. The EM structures, obtained in this study, cover all main conformations. The new UR^{asym} conformations have closest resemblance to OF^{occluded}. The IC angle is defined as the angle between two vectors: vector 1 between the center of mass of the whole extracellular part of the TMD region and the center of mass of the intracellular parts of TM1^{TmrA}, TM2^{TmrA}, TM3^{TmrA}, TM6^{TmrA}, TM4^{TmrB}, and TM5^{TmrB}; and vector 2 between the center of mass of the whole extracellular part of the TMD region and the center of mass of the intracellular parts of TM1^{TmrB}, TM2^{TmrB}, TM3^{TmrB}, TM6^{TmrB}, TM4^{TmrA}, and TM5^{TmrA}. The EC angle is defined as the angle between two vectors: vector 3 between the centers of mass of the NBDs and the extracellular parts TM1^{TmrA}, TM2^{TmrA}, TM3^{TmrB}, TM4^{TmrB}, TM5^{TmrB}, and TM6^{TmrB}; and vector 4 between the center of mass of the NBDs and of the extracellular parts TM1^{TmrB}, TM2^{TmrB}, TM3^{TmrA}, TM4^{TmrA}, TM5^{TmrA}, and TM6^{TmrA}. The NBD distance is defined by the centers of mass of two NBDs (N-terminal loops and C-terminal helices were excluded). IF: IF conformation; O: OF^{open} conformation; C: OF^{occluded} conformation; Vi: TmrAB_{ATP-Vi}; EQ: TmrA^{EQB}. PDB IDs: PCAT: 4RY2 and

4S0F for the IF and OF^{occluded} conformation, respectively⁵¹; McjD: 4PL0¹⁶; Pgp: 6C0V⁵²; MsbA: 5TTP⁵³; PglK: 5C73⁵⁴; MRP: 6BHU⁵⁵; Sav: 2ONJ¹⁸; TmrAB: 5MKK¹²; TM287 (TM287/288): 4Q4A⁵⁶. **d**, Time-dependent IC angle in independent MD simulations of IF^{wide} and IF^{narrow} with ATP/ATP, ADP/ATP, and ADP/ADP in the canonical/non-canonical site, respectively.

Extended Data Table 1
Cryo-EM data collection, refinement and validation statistics.

* Number of particles after two rounds of 3D classification to remove false positives

	Turnover IF ^{narrow}	Turnover IF ^{wide}	EQ OF ^{open}	EQ OF ^{occluded}	ATP-Vi OF ^{open}	ATP-Vi OF ^{occluded}	Turnover UR ^{asym}	Turnover UR ^{asym*}
Turnover IF ^{narrow}	0.00	2.78	8.00	7.08	8.08	7.13	6.82	6.48
Turnover IF ^{wide}	2.27	0.00	7.54	6.51	7.61	6.55	6.15	5.74
EQ OF ^{open}	5.85	6.33	0.00	3.71	0.71	3.65	3.72	3.98
EQ OF ^{occluded}	3.83	4.39	4.61	0.00	3.79	0.64	0.82	1.32
ATP-Vi OF ^{open}	5.86	6.35	0.70	4.64	0.00	3.70	3.83	4.05
ATP-Vi OF ^{occluded}	3.88	4.44	4.54	0.64	4.57	0.00	0.92	1.42
Turnover UR ^{asym}	3.46	3.98	4.62	0.75	4.65	0.85	0.00	0.90
Turnover UR ^{asym*}	3.04	3.53	4.78	1.18	4.80	1.25	0.78	0.00

Extended Data Table 2 RMSD of overall structure (blue) and TMD region (orange).

Superposition was performed at backbone level and RMSD was calculated at the C_{α} level. N_{term} elbow and C_{term} zipper helices were excluded from the superimposition and RMSD calculation. RMSD values of 0.64 Å and 0.70 Å show that the OF^{open} and OF^{occluded} conformations determined from the $TmrAB_{\text{ATP-Vi}}$ and $TmrA^{EOB}_{\text{ATP}}$ datasets, respectively, are very similar.

	$TmrAB_{\text{turnover}}$ rAB_{turnover} IF^{turnover} (EMD-4773) (PDB 6RAF)	$TmrAB_{\text{turnover}}$ IF^{wide} (EMD-4774) (PDB 6RAG)	$TmrAB_{\text{turnover}}$ UR^{asym} (EMD-4779) (PDB 6RAL)	$TmrAB_{\text{turnover}}$ UR^{asym} (EMD-4780) (PDB 6RAM)	$TmrA^{EOB}_{\text{ATP-ADP}}$ IF^{wide} (EMD-4781) (PDB 6RAN)	$TmrA^{EOB}_{\text{ATP-ADP}}$ OF^{open} (EMD-4775) (PDB 6RAH)	$TmrA^{EOB}_{\text{ATP-ADP}}$ OF^{occluded} (EMD-4776) (PDB 6RAI)	$TmrA_{\text{ATP-Vi}}$ OF^{open} (EMD-4777) (PDB 6RAJ)	$TmrA_{\text{ATP-Vi}}$ OF^{occluded} (EMD-4778) (PDB 6RAK)
Data collection and processing									
Microscope	Titan Krios G2	Titan Krios G2	Titan Krios G2	Titan Krios G2	Titan Krios G2	Titan Krios G2	Titan Krios G2	Titan Krios G2	Titan Krios G2
Camera	GIF Quantum K2	GIF Quantum K2	GIF Quantum K2	GIF Quantum K2	GIF Quantum K2	GIF Quantum K2	GIF Quantum K2	GIF Quantum K2	GIF Quantum K2
Magnification	130,000	130,000	130,000	130,000	130,000	130,000	130,000	130,000	130,000
Voltage (kV)	300	300	300	300	300	300	300	300	300
Electron exposure ($e^-/\text{Å}^2$)	62	62	62	62	62	64	64	64	64
Defocus range (μm)	-0.8 to -2.8	-0.8 to -2.8	-0.8 to -2.8	-0.8 to -2.8	-0.8 to -2.8	-0.8 to -2.8	-0.8 to -2.8	-0.5 to -2.5	-0.5 to -2.5
Pixel size (Å)	1.077	1.077	1.077	1.077	1.077	1.077	1.077	1.077	1.077
Symmetry imposed	CI	CI	CI	CI	CI	CI	CI	CI	CI
Initial particle images (no.)	4,043,869	4,043,869	4,043,869	4,043,869	2,126,064	2,355,206	2,355,206	1,304,264	1,304,264
Final particle images (no.)	133,527	208,674	145,913	97,763	(418,392)*	(1,420,676)*	(1,420,676)*	(358,656)*	109,080
Map resolution (Å)	3.8	4.2	3.5	3.8	4.2	2.8	2.9	3.5	3.3
FSC threshold	0.143	0.143	0.143	0.143	0.143	0.143	0.143	0.143	0.143
Map resolution range (Å)	3.4-6.5	3.6-7.8	3.0-5.0	3.4-6.4	3.8-7.1	2.7-4.0	2.7-4.0	3.2-5.5	2.9-4.0
Refinement									
Initial model used (PDB code)	5MKK	5MKK	5MKK/4PLO	5MKK/4PLO	5MKK	5MKK/2ONJ	5MKK/4PLO	5MKK/2ONJ	5MKK/4PLO

	T_m rAB_{turnover} IF_{marlow} (EMD-4773) (PDB 6RAF)	TmrAB_{turnover} IF_{wide} (EMD-4774) (PDB 6RAG)	TmrAB_{turnover} UR_{asym} (EMD-4779) (PDB 6RAL)	TmrAB_{turnover} UR_{asym} (EMD-4780) (PDB 6RAM)	TmrA_{QB_Caf} IF_{wide} (EMD-4781) (PDB 6RAN)	TmrA_{EQB_ATP-ADP} OF_{open} (EMD-4775) (PDB 6RAH)	TmrA_{EQB_ATP-ADP} OF_{occluded} (EMD-4776) (PDB 6RAI)	TmrAB_{ATP_i} OF_{open} (EMD-4777) (PDB 6RAJ)	TmrAB_{ATP_i} OF_{occluded} (EMD-4778) (PDB 6RAK)
Model resolution (Å)	3.8	4.2	3.5	3.8	4.2	2.8	2.9	3.5	3.3
FSC threshold	0.143	0.143	0.143	0.143	0.143	0.143	0.143	0.143	0.143
Map sharpening <i>B</i> factor (Å ²)	-110	-100	-100	-106	-100	-46	-54	-100	-95
Model composition									
Non-hydrogen atoms	10174	10188	10127	10186	10173	10161	10191	10198	10180
Protein residues	1280	1282	1275	1281	1287	1278	1281	1282	1280
Nucleotides	2	2	2	2	-	2	2	2	2
Water molecules	-	-	-	-	-	4	6	-	-
<i>B</i> factors (Å ²)									
Protein	81.4	112.6	58.8	110.0	107.4	73.9	55.7	72.5	41.9
Nucleotides	99.2	150.4	56.4	113.3	-	52.4	44.1	56.6	32.6
Water molecules	-	-	-	-	-	49.4	43.5	---	---
R.m.s. deviations									
Bond lengths (Å)	0.0078	0.0096	0.0063	0.0164	0.0167	0.0078	0.0084	0.0079	0.0054
Bond angles (°)	1.55	1.38	1.15	1.94	2.08	1.53	1.35	1.08	1.02
Validation									
MolProbity score	1.59	1.84	1.77	1.72	1.76	1.58	1.71	1.48	1.48
Clashscore	6.17	10.72	8.15	10.48	9.74	10.02	9.27	4.94	5.19
Poor rotamers (%)	0.10	0.67	0.00	0.10	0.09	0.00	0.00	0.19	0.00
Ramachandran plot									
Favored (%)	96.23	95.85	95.35	96.94	96.25	97.72	96.63	96.55	96.78
Outliers (%)	0.31	0.00	0.08	0.24	0.08	0.16	0.00	0.00	0.00

Supplementary Material

Refer to Web version on PubMed Central for supplementary material.

Acknowledgements

This research was supported by the German Research Foundation (Mo2752/2 to A.M., SFB 807 – Membrane Transport and Communication to E.R.G., G.H., A.M. and R.T., and Cluster of Excellence Frankfurt EXC 115 – Macromolecular Complexes to E.R.G., G.H., A.M. and R.T.). D.J., A.R.M., G.H., and A.M. acknowledge support by the Max Planck Society. R.T. is grateful for the support by an ERC Advanced Grant. We acknowledge W. Kühlbrandt and D. Mills for access to the excellent cryo-EM facility at the MPI of Biophysics funded by the Max Planck Society. We acknowledge K. Holztüter for creating the nanobody libraries, S. Štefani from the Nanobody Service Facility (University of Zurich) for alpaca immunization and lymphocyte isolation. We thank all members of the Institute of Biochemistry (Goethe University Frankfurt) and the staff at the Department of Structural Biology (MPI of Biophysics) for discussions and comments on the manuscript.

References

- Henderson R. Realizing the potential of electron cryo-microscopy. *Q Rev Biophys.* 2004; 37: 3–13. [PubMed: 17390603]
- Frank J. New opportunities created by single-particle cryo-EM: the mapping of conformational space. *Biochemistry.* 2018; 57: 888–888. [PubMed: 29368918]
- Cheng Y. Single-particle cryo-EM-How did it get here and where will it go. *Science.* 2018; 361: 876–880. [PubMed: 30166484]
- Rees DC, Johnson E, Lewinson O. ABC transporters: the power to change. *Nat Rev Mol Cell Biol.* 2009; 10: 218–227. [PubMed: 19234479]
- Locher KP. Mechanistic diversity in ATP-binding cassette (ABC) transporters. *Nat Struct Mol Biol.* 2016; 23: 487–493. [PubMed: 27273632]
- Thomas C, Tampé R. Multifaceted structures and mechanisms of ABC transport systems in health and disease. *Curr Opin Struct Biol.* 2018; 51: 116–128. [PubMed: 29635113]
- Robey RW, et al. Revisiting the role of ABC transporters in multidrug-resistant cancer. *Nat Rev Cancer.* 2018; 18: 452–464. [PubMed: 29643473]
- Trowitzsch S, Tampé R. ABC transporters in dynamic macromolecular assemblies. *J Mol Biol.* 2018; 430: 4481–4495. [PubMed: 30089236]
- Dean M, Annilo T. Evolution of the ATP-binding cassette (ABC) transporter superfamily in vertebrates. *Annu Rev Genomics Hum Genet.* 2005; 6: 123–142. [PubMed: 16124856]
- Zutz A, et al. Asymmetric ATP hydrolysis cycle of the heterodimeric multidrug ABC transport complex TmrAB from *Thermus thermophilus*. *J Biol Chem.* 2011; 286: 7104–7115. [PubMed: 21190941]
- Kim J, et al. Subnanometre-resolution electron cryomicroscopy structure of a heterodimeric ABC exporter. *Nature.* 2015; 517: 396–400. [PubMed: 25363761]
- Nöll A, et al. Crystal structure and mechanistic basis of a functional homolog of the antigen transporter TAP. *Proc Natl Acad Sci U S A.* 2017.
- Alam A, Kowal J, Broude E, Roninson I, Locher KP. Structural insight into substrate and inhibitor discrimination by human P-glycoprotein. *Science.* 2019; 363: 753–756. [PubMed: 30765569]
- Dey S, Ramachandra M, Pastan I, Gottesman MM, Ambudkar SV. Evidence for two nonidentical drug-interaction sites in the human P-glycoprotein. *Proc Natl Acad Sci U S A.* 1997; 94: 10594–10599. [PubMed: 9380680]
- Grossmann N, et al. Mechanistic determinants of the directionality and energetics of active export by a heterodimeric ABC transporter. *Nat Commun.* 2014; 5: 5419. [PubMed: 25377891]
- Choudhury HG, et al. Structure of an antibacterial peptide ATP-binding cassette transporter in a novel outward occluded state. *Proc Natl Acad Sci U S A.* 2014; 111: 9145–9150. [PubMed: 24920594]

17. Dawson RJ, Locher KP. Structure of a bacterial multidrug ABC transporter. *Nature*. 2006; 443: 180–185. [PubMed: 16943773]
18. Dawson RJ, Locher KP. Structure of the multidrug ABC transporter Sav1866 from *Staphylococcus aureus* in complex with AMP-PNP. *FEBS Lett*. 2007; 581: 935–938. [PubMed: 17303126]
19. Zaitseva J, et al. A structural analysis of asymmetry required for catalytic activity of an ABC-ATPase domain dimer. *EMBO J*. 2006; 25: 3432–3443. [PubMed: 16858415]
20. Oldham ML, Chen J. Snapshots of the maltose transporter during ATP hydrolysis. *Proc Natl Acad Sci U S A*. 2011; 108: 15152–15156. [PubMed: 21825153]
21. Yang M, et al. Single-molecule probing of the conformational homogeneity of the ABC transporter BtuCD. *Nat Chem Biol*. 2018; 14: 715–722. [PubMed: 29915236]
22. Verhalen B, et al. Energy transduction and alternating access of the mammalian ABC transporter P-glycoprotein. *Nature*. 2017; 543: 738–741. [PubMed: 28289287]
23. Watanabe R, Iino R, Noji H. Phosphate release in F1-ATPase catalytic cycle follows ADP release. *Nat Chem Biol*. 2010; 6: 814–820. [PubMed: 20871600]
24. Okazaki K, Hummer G. Phosphate release coupled to rotary motion of F1-ATPase. *Proc Natl Acad Sci U S A*. 2013; 110: 16468–16473. [PubMed: 24062450]
25. Catipovic MA, Bauer BW, Loparo JJ, Rapoport TA. Protein translocation by the SecA ATPase occurs by a power-stroke mechanism. *EMBO J*. 2019; 38
26. Roos C, et al. Characterization of co-translationally formed nanodisc complexes with small multidrug transporters, proteorhodopsin and with the *E. coli* MraY translocase. *Biochim Biophys Acta*. 2012; 1818: 3098–3106. [PubMed: 22960287]
27. Ehrnstorfer IA, Geertsma ER, Pardon E, Steyaert J, Dutzler R. Crystal structure of a SLC11 (NRAMP) transporter reveals the basis for transition-metal ion transport. *Nat Struct Mol Biol*. 2014; 21: 990–996. [PubMed: 25326704]
28. Pardon E, et al. A general protocol for the generation of Nanobodies for structural biology. *Nat Protoc*. 2014; 9: 674–693. [PubMed: 24577359]
29. Zimmermann I, et al. Synthetic single domain antibodies for the conformational trapping of membrane proteins. *Elife*. 2018; 7
30. Gewering T, Janulienė D, Ries AB, Moeller A. Know your detergents: A case study on detergent background in negative stain electron microscopy. *J Struct Biol*. 2018; 203: 242–246. [PubMed: 29852220]
31. Suloway C, et al. Automated molecular microscopy: the new Legion system. *J Struct Biol*. 2005; 151: 41–60. [PubMed: 15890530]
32. Tegunov D, Cramer P. Real-time cryo-EM data pre-processing with Warp. *bioRxiv*. 2018.
33. Zivanov J, et al. New tools for automated high-resolution cryo-EM structure determination in RELION-3. *Elife*. 2018; 7
34. Zheng SQ, et al. MotionCor2: anisotropic correction of beam-induced motion for improved cryo-electron microscopy. *Nat Methods*. 2017; 14: 331–332. [PubMed: 28250466]
35. Zhang K. Gctf: Real-time CTF determination and correction. *J Struct Biol*. 2016; 193: 1–12. [PubMed: 26592709]
36. Punjani A, Rubinstein JL, Fleet DJ, Brubaker MA. cryoSPARC: algorithms for rapid unsupervised cryo-EM structure determination. *Nat Methods*. 2017; 14: 290–296. [PubMed: 28165473]
37. Larkin MA, et al. Clustal W and Clustal X version 2.0. *Bioinformatics*. 2007; 23: 2947–2948. [PubMed: 17846036]
38. Sali A, Blundell TL. Comparative protein modelling by satisfaction of spatial restraints. *J Mol Biol*. 1993; 234: 779–815. [PubMed: 8254673]
39. Phillips JC, et al. Scalable molecular dynamics with NAMD. *J Comput Chem*. 2005; 26: 1781–1802. [PubMed: 16222654]
40. Singharoy A, et al. Molecular dynamics-based refinement and validation for sub-5 Å cryo-electron microscopy maps. *Elife*. 2016; 5
41. Emsley P, Lohkamp B, Scott WG, Cowtan K. Features and development of Coot. *Acta Crystallogr D Biol Crystallogr*. 2010; 66: 486–501. [PubMed: 20383002]

42. Adams PD, et al. PHENIX: a comprehensive Python-based system for macromolecular structure solution. *Acta Crystallogr D Biol Crystallogr*. 2010; 66: 213–221. [PubMed: 20124702]
43. Chen VB, et al. MolProbity: all-atom structure validation for macromolecular crystallography. *Acta Crystallogr D Biol Crystallogr*. 2010; 66: 12–21. [PubMed: 20057044]
44. Laskowski RA, MacArthur MW, Moss DS, Thornton JM. PROCHECK: a program to check the stereochemical quality of protein structures. *J Appl Crystallogr*. 1993; 26: 283–291.
45. Wu EL, et al. CHARMM-GUI Membrane Builder toward realistic biological membrane simulations. *J Comput Chem*. 2014; 35: 1997–2004. [PubMed: 25130509]
46. Best RB, et al. Optimization of the additive CHARMM all-atom protein force field targeting improved sampling of the backbone phi, psi and side-chain chi(1) and chi(2) dihedral angles. *J Chem Theory Comput*. 2012; 8: 3257–3273. [PubMed: 23341755]
47. Abraham MJ, et al. GROMACS: High performance molecular simulations through multi-level parallelism from laptops to supercomputers. *SoftwareX*. 2015; 1: 19–25.
48. Han W, Cheng RC, Maduke MC, Tajkhorshid E. Water access points and hydration pathways in CLC H+/Cl⁻ transporters. *Proc Natl Acad Sci U S A*. 2014; 111: 1819–1824. [PubMed: 24379362]
49. Khelashvili G, et al. Conformational dynamics on the extracellular side of LeuT controlled by Na⁺ and K⁺ ions and the protonation state of Glu290. *J Biol Chem*. 2016; 291: 19786–19799. [PubMed: 27474737]
50. Zhao C, Noskov SY. The role of local hydration and hydrogen-bonding dynamics in ion and solute release from ion-coupled secondary transporters. *Biochemistry*. 2011; 50: 1848–1856. [PubMed: 21265577]
51. Lin DY, Huang S, Chen J. Crystal structures of a polypeptide processing and secretion transporter. *Nature*. 2015; 523: 425–430. [PubMed: 26201595]
52. Kim Y, Chen J. Molecular structure of human P-glycoprotein in the ATP-bound, outward-facing conformation. *Science*. 2018; 359: 915–919. [PubMed: 29371429]
53. Mi W, et al. Structural basis of MsbA-mediated lipopolysaccharide transport. *Nature*. 2017; 549: 233–237. [PubMed: 28869968]
54. Perez C, et al. Structure and mechanism of an active lipid-linked oligosaccharide flippase. *Nature*. 2015; 524: 433–438. [PubMed: 26266984]
55. Johnson ZL, Chen J. ATP binding enables substrate release from multidrug resistance protein 1. *Cell*. 2018; 172: 81–89 e10. [PubMed: 29290467]
56. Hohl M, et al. Structural basis for allosteric cross-talk between the asymmetric nucleotide binding sites of a heterodimeric ABC exporter. *Proc Natl Acad Sci U S A*. 2014; 111: 11025–11030. [PubMed: 25030449]

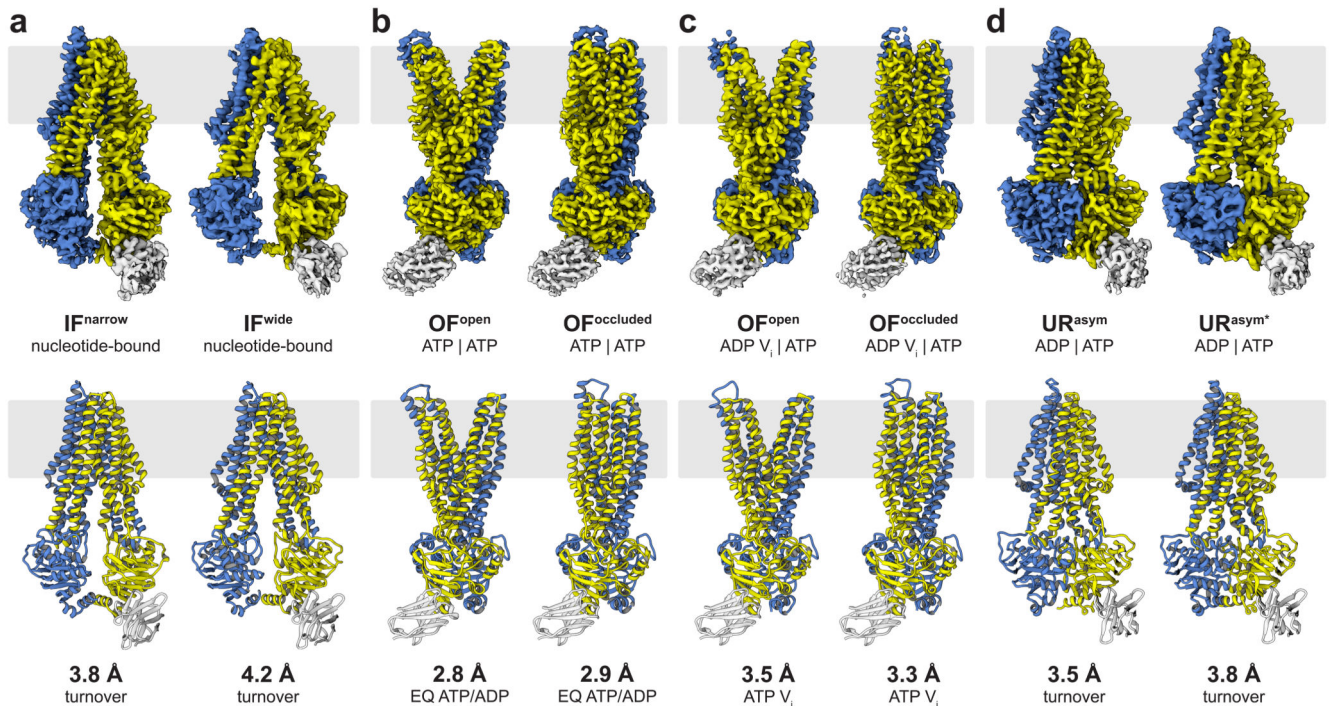


Figure 1. The conformational space of TmrAB.

a, Two distinct IF conformations from TmrAB_{turnover}. In IF^{wide}, the intracellular gate has opened by 4.4 Å, allowing access for bulky substrates. Wide and narrow IF conformations were also found in the control datasets and in absence of nucleotides and/or substrate. Densities for nucleotides were observed in all IF conformations in TmrAB_{turnover} and TmrA^{EQB}_{ATP-ADP} datasets, but not in TmrAB_{apo} and TmrAB_{C4F}, as no nucleotides were added in the latter cases. **b**, In the ATP-bound state, the NBDs are tightly dimerized and the exporter exhibits either an OF^{open} or OF^{occluded} conformation. The same two OF conformations are observed in both TmrA^{EQB}_{ATP} and TmrA^{EQB}_{ATP-ADP} datasets (E523Q mutation in TmrA); therefore, only maps from TmrA^{EQB}_{ATP-ADP} are shown here due to the higher resolution. **c**, OF^{open} and OF^{occluded} conformations also dominate in the vanadate-trapped state. **d**, The asymmetric states from TmrAB_{turnover} resemble an OF^{occluded} conformation with a slightly separated NBD interface. In contrast to the OF^{occluded} conformations of TmrA^{EQB}_{ATP-ADP} and TmrAB_{ATP-V_i}, the intracellular gate is opened by 1.5 Å and 3.0 Å in UR^{asym} and UR^{asym*}, respectively, while the extracellular gate is tightly sealed. The top and bottom rows show experimental maps and deposited models, respectively. OF densities and models in **b** and **c** are rotated by 90° with respect to panel **a** and **d** to illustrate the opening of the extracellular gate. TmrA is blue, TmrB yellow, and the nanobody light grey. All structures and morphs between conformers are highlighted in the Supplementary Video 1 and 2.

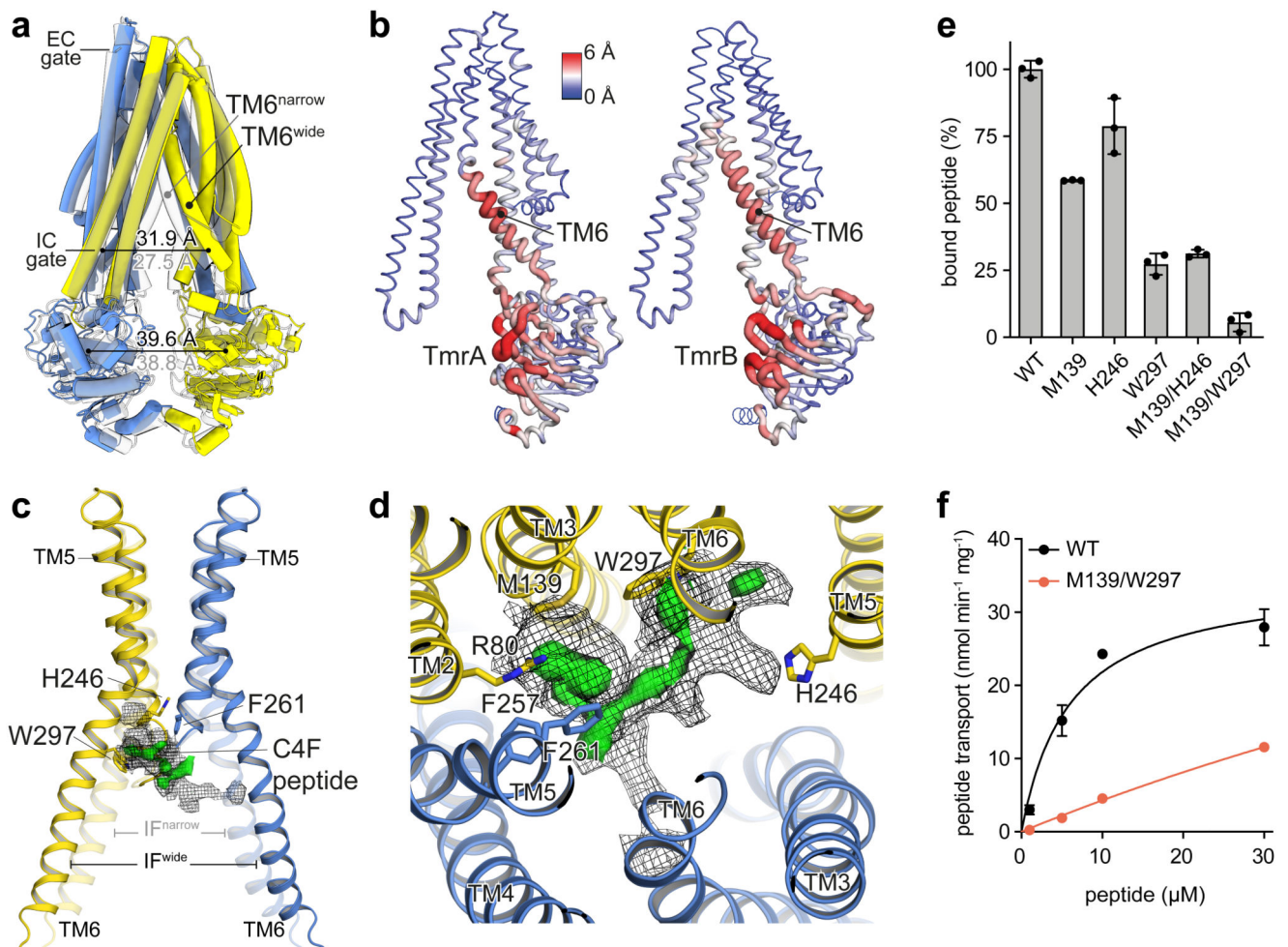


Figure 2. Conformational plasticity in IF conformations translates to substrate binding.
a, Superposition of the IF^{narrow} (grey) and IF^{wide} conformation illustrating the displacement of TM6. In IF^{wide}, the intracellular (IC) gate opens by 4.4 Å, while the inter-NBD distance (center of mass) changes only marginally. TmrA is blue, TmrB yellow. **b**, The TM6 gatekeeper helix and the NBD interface show highest conformational variability in the IF state. Red color and wide tubes indicate large C α distances between IF^{narrow} and IF^{wide} in a backbone superposition, excluding the N-terminal elbow and C-terminal helices. **c**, Superposition of IF^{wide} and IF^{narrow} (transparent) and focussed representation of the substrate-binding region of TmrAB highlights the widening of the binding cavity upon displacement of TM6. The helix acts as a gatekeeper for substrate uptake, blocking binding of bulky substrates in the narrow conformation. The calculated difference map ($F_{obs} - F_{calc}$; green) is overlaid with the experimental density (mesh) at a lower threshold to illustrate the extent of the putative peptide density. **d**, Focussed top view with cryo-EM density (mesh) and positive difference density (green surface) in the binding site of IF^{wide} (TmrAB_{C4F}), as also identified in TmrAB_{turnover}, but not in TmrAB_{apo}. Nearby residues are depicted as sticks colored by heteroatoms. **e**, Alanine substitutions in TmrB reduce substrate binding, as analyzed by fluorescence polarization of 50 nM C4F peptide and 2 µM TmrAB. **f**, Peptide

transport kinetics of TmrAB^{WT} (black) and double alanine mutant (red) show an additive effect. Binding and transport data represent mean \pm SD from three experiments.

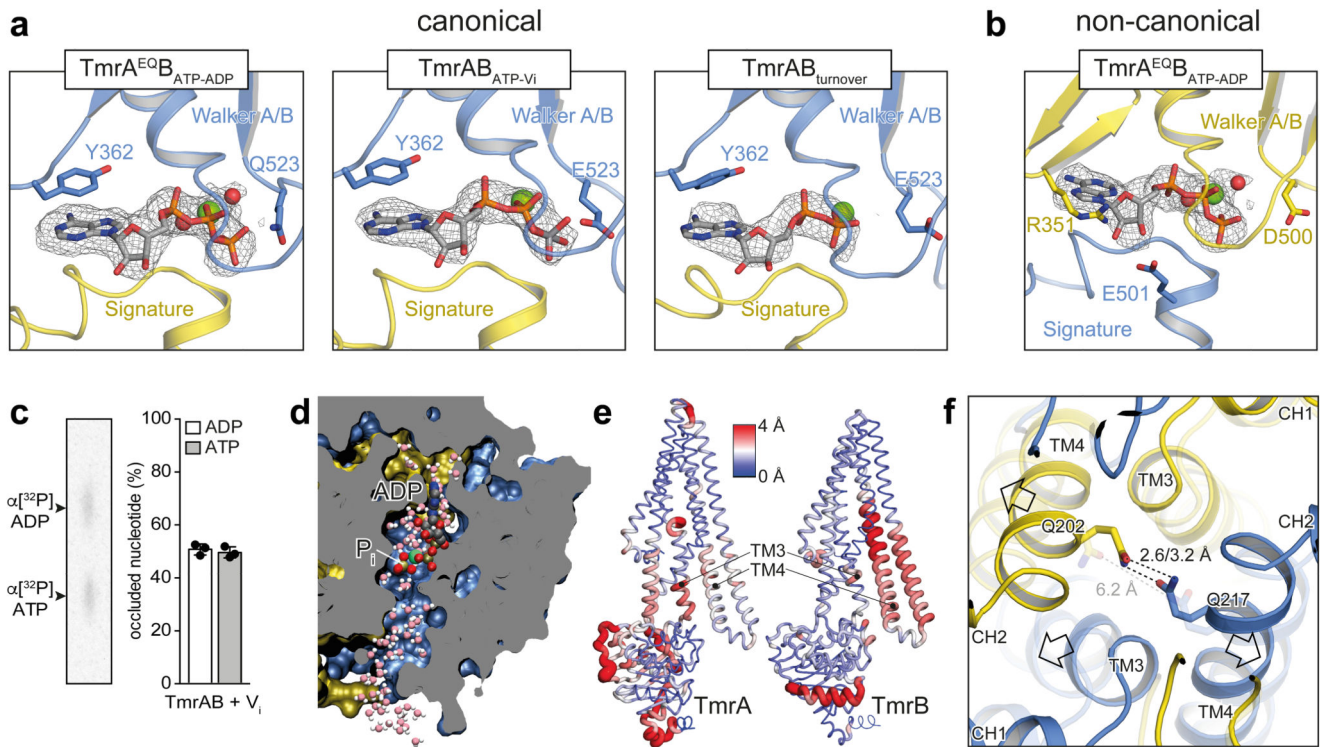


Figure 3. Nucleotide states in the sandwiched NBD dimer and opening of the intracellular gate.

a. Different nucleotide states were observed at the canonical nucleotide-binding site in the conformations with dimerized NBDs from TmrA^{EQB}_{ATP-ADP}, TmrAB_{ATP-Vi}, and TmrAB_{turnover} (highest resolution map presented). In all cases, the nucleotide-binding pocket is aligned by the conserved Walker A/B motives and the signature motif. Mg²⁺ and water molecules are shown as green and red spheres, respectively. TmrA is blue, TmrB yellow. **b.** The non-canonical site is occupied by ATP in all examples, as hydrolysis cannot proceed. OF^{open} from TmrA^{EQB}_{ATP-ADP} is shown as an example. In the non-canonical site, the sugar moiety of the bound nucleotide interacts with R351^{TmrB} and E501^{TmrA}, while a tyrosine residue (Y362^{TmrA}) makes π - π stacking contacts with the purine base in the canonical site. **c.** The stoichiometric occlusion of ADP and ATP was validated by thin-layer chromatography upon vanadate-trapping of TmrAB^{WT} (mean \pm SD from three experiments). **d.** MD snapshot showing two possible exit pathways for inorganic phosphate (P_i) after hydrolysis in a cut through the NBD dimer. P_i can escape through hydrated channels directed towards the C-terminal helices (bottom) and the coupling helix (top). The OF^{occluded} conformation of TmrAB_{ATP-Vi} was simulated with bound ADP and P_i (HPO₄²⁻). **e.** The NBD dimer, TM3, and TM4 show the largest differences between OF^{occluded} and UR^{asym*} conformations. Red color and wide tubes indicate large Ca distances. The distances were averaged over two OF^{occluded} (from TmrA^{EQB}_{ATP-ADP} and TmrAB_{ATP-Vi}) and the UR^{asym*} conformation in a backbone superposition excluding the N-terminal elbow and C-terminal helices. The TM3 and TM4 motions from OF to UR^{asym*} progressively separate the intracellular gate. **f.** After P_i release, the intracellular gate lined by TM4

and TM3 of each subunit is unlocked, forming the asymmetric turnover state UR^{asym*} . $OF^{occluded}$ is transparent.

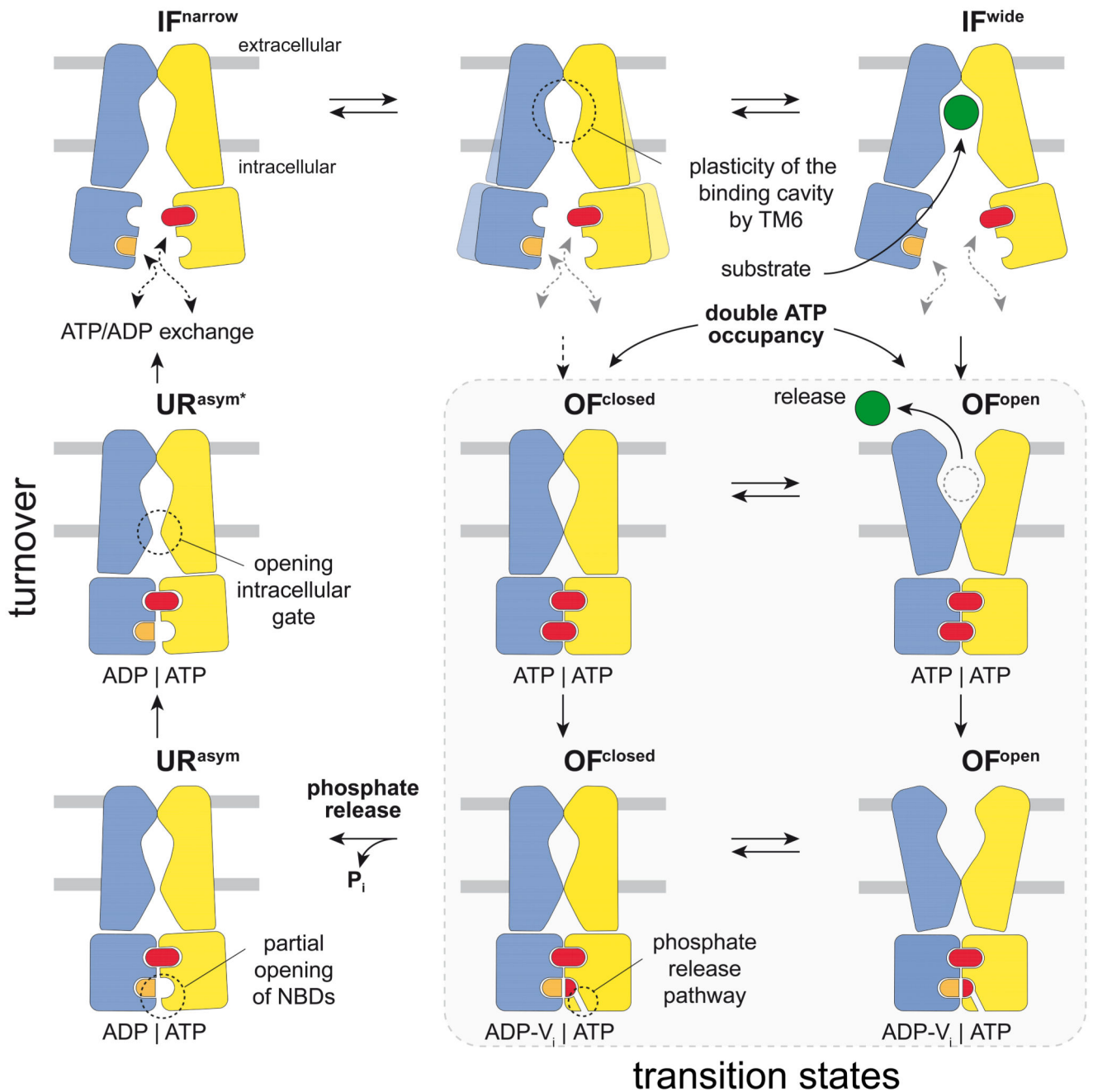


Figure 4. Translocation cycle of the heterodimeric ABC exporter TmrAB.

TmrAB fluctuates between IF^{narrow} and IF^{wide} with TM6 acting as gatekeeper, controlling access and volume of the substrate-binding cavity. Therefore, bulky substrates can only bind to the IF^{wide} conformation. Independent of substrate binding and IF conformation, ATP binding to both NBDs induces NBD dimerization, which closes the intracellular gate and allows the extracellular gate to open. After substrate release, TmrAB can isomerize between OF^{open} and $OF^{occluded}$ conformations in the ATP-bound state until P_i is discharged from the canonical site. P_i release via a phosphate channel results in an asymmetric UR^{asym}

conformation and triggers partial opening of the NBDs and the intracellular gate, which advances the exporter towards the IF conformation. Separation of the NBD dimer by dissociation of the ATP-bound non-canonical site represents the rate-limiting step during the cycle. Conceivably, ATP binding can also lead directly to an OF^{occluded} conformation. In this case bulky substrates cannot be transported, indicating either a futile cycle or one designated for small, amphipathic molecules, that do not require opening of the extracellular gate for transport. TmrA and TmrB are shown in blue and yellow, respectively.

Extended Data Table 2

RMSD of overall structure (blue) and TMD region (orange).

Superposition was performed at backbone level and RMSD was calculated at the C_α level. N_{term} elbow and C_{term} zipper helices were excluded from the superimposition and RMSD calculation. RMSD values of 0.64 Å and 0.70 Å show that the OF_{open} and OF_{occluded} conformations determined from the $\text{TmrAB}_{\text{ATP-Vi}}$ and $\text{TmrA}^{EQB}_{\text{ATP}}$ datasets, respectively, are very similar.

	$\text{TmrAB}_{\text{turnover}}$ $IF_{\text{narrow}}^{\text{turnover}}$ (EMD-4773) (PDB 6RAF)	$\text{TmrAB}_{\text{turnover}}$ $IF_{\text{wide}}^{\text{turnover}}$ (EMD-4774) (PDB 6RAG)	$\text{TmrAB}_{\text{turnover}}$ UR_{asym} (EMD-4779) (PDB 6RAL)	$\text{TmrAB}_{\text{turnover}}$ UR_{asym}^* (EMD-4780) (PDB 6RAM)	$\text{TmrA}^{EQB}_{\text{CF}}$ IF_{wide} (EMD-4781) (PDB 6RAH)	$\text{TmrA}^{EQB}_{\text{ATP-ADP}}$ OF_{open} (EMD-4775) (PDB 6RAH)	$\text{TmrA}^{EQB}_{\text{ATP-ADP}}$ OF_{occluded} (EMD-4776) (PDB 6RAI)	$\text{TmrAB}_{\text{ATP-Vi}}$ OF_{open} (EMD-4777) (PDB 6RAJ)	$\text{TmrAB}_{\text{ATP-Vi}}$ OF_{occluded} (EMD-4778) (PDB 6RAK)
Microscope	Titan Krios G2	Titan Krios G2	Titan Krios G2	Titan Krios G2	Titan Krios G2	Titan Krios G2	Titan Krios G2	Titan Krios G2	Titan Krios G2
Camera	GIF Quantum K2	GIF Quantum K2	GIF Quantum K2	GIF Quantum K2	GIF Quantum K2	GIF Quantum K2	GIF Quantum K2	GIF Quantum K2	GIF Quantum K2
Magnification	130,000	130,000	130,000	130,000	130,000	130,000	130,000	130,000	130,000
Voltage (kV)	300	300	300	300	300	300	300	300	300
Electron exposure ($e^-/\text{Å}^2$)	62	62	62	62	62	64	64	64	64
Defocus range (μm)	-0.8 to -2.8	-0.8 to -2.8	-0.8 to -2.8	-0.8 to -2.8	-0.8 to -2.8	-0.8 to -2.8	-0.8 to -2.8	-0.5 to -2.5	-0.5 to -2.5
Pixel size (Å)	1.077	1.077	1.077	1.077	1.077	1.077	1.077	1.077	1.077
Symmetry imposed	CI	CI	CI	CI	CI	CI	CI	CI	CI
Initial particle images (no.)	4,043,869	4,043,869	4,043,869	4,043,869	2,126,064	2,355,206	2,355,206	1,304,264	1,304,264
Final particle images (no.)	(2,340,747)*	(2,340,747)*	(2,340,747)*	(2,340,747)*	(418,392)*	(1,420,676)*	(1,420,676)*	(358,656)*	(358,656)*
Map resolution (Å)	133,527	208,674	145,913	97,763	44,733	60,950	94,621	44,051	109,080
Map resolution (Å)	3.8	4.2	3.5	3.8	4.2	2.8	2.9	3.5	3.3
FSC threshold	0.143	0.143	0.143	0.143	0.143	0.143	0.143	0.143	0.143
Map resolution range (Å)	3.4-6.5	3.6-7.8	3.0-5.0	3.4-6.4	3.8-7.1	2.7-4.0	2.7-4.0	3.2-5.5	2.9-4.0
Refinement									
Initial model used (PDB code)	5MKK	5MKK	5MKK/4PLO	5MKK/4PLO	5MKK	5MKK/2ONJ	5MKK/4PLO	5MKK/2ONJ	5MKK/4PLO
Model resolution (Å)	3.8	4.2	3.5	3.8	4.2	2.8	2.9	3.5	3.3
FSC threshold	0.143	0.143	0.143	0.143	0.143	0.143	0.143	0.143	0.143
Map sharpening B factor (Å^2)	-110	-100	-100	-106	-100	-46	-54	-100	-95
Model composition									
Non-hydrogen atoms	10174	10188	10127	10186	10173	10161	10191	10198	10180
Protein residues	1280	1282	1275	1281	1287	1278	1281	1282	1280
Nucleotides	2	2	2	2	-	2	2	2	2

	TmrAB _{turnover} IF _{narrow} (EMD-4773) (PDB 6RAF)	TmrAB _{turnover} IF _{wide} (EMD-4774) (PDB 6RAC)	TmrAB _{turnover} UR _{syn} (EMD-4779) (PDB 6RAL)	TmrAB _{turnover} UR _{syn} (EMD-4780) (PDB 6RAM)	TmrA ^{EQB} _{ADP} OF _{open} (EMD-4775) (PDB 6RAH)	TmrA ^{EQB} _{ADP} OF _{closed} (EMD-4776) (PDB 6RAI)	TmrA ^{EQB} _{ATP} OF _{open} (EMD-4777) (PDB 6RAJ)	TmrA ^{EQB} _{ATP} OF _{closed} (EMD-4778) (PDB 6RAK)
Water molecules	-	-	-	-	4	6	-	-
<i>B</i> factors (Å ²)								
Protein	81.4	112.6	58.8	110.0	73.9	55.7	72.5	41.9
Nucleotides	99.2	150.4	56.4	113.3	52.4	44.1	56.6	32.6
Water molecules	-	-	-	-	49.4	43.5	---	---
R.m.s. deviations								
Bond lengths (Å)	0.0078	0.0096	0.0063	0.0164	0.0078	0.0084	0.0079	0.0054
Bond angles (°)	1.55	1.38	1.15	1.94	1.53	1.35	1.08	1.02
Validation								
MolProbity score	1.59	1.84	1.77	1.72	1.58	1.71	1.48	1.48
Clashscore	6.17	10.72	8.15	10.48	10.02	9.27	4.94	5.19
Poor rotamers (%)	0.10	0.67	0.00	0.10	0.00	0.00	0.19	0.00
Ramachandran plot								
Favored (%)	96.23	95.85	95.35	96.94	97.72	96.63	96.55	96.78
Outliers (%)	0.31	0.00	0.08	0.24	0.16	0.00	0.00	0.00